

# A Blueprint for the Milky Way’s Stellar Populations. IV. Spectrum-based Empirical Corrections and the Galactic Starburst Sequence

DEOKKEUN AN,<sup>1</sup> TIMOTHY C. BEERS,<sup>2</sup> YOUNG SUN LEE,<sup>2,3</sup> AND THOMAS MASSERON<sup>4,5</sup>

<sup>1</sup>*Department of Science Education, Ewha Womans University, 52 Ewhayeodae-gil, Seodaemun-gu, Seoul 03760, Republic of Korea; deokkeun@ewha.ac.kr*

<sup>2</sup>*Department of Physics and Astronomy and JINA Center for the Evolution of the Elements, University of Notre Dame, Notre Dame, IN 46556, USA*

<sup>3</sup>*Department of Astronomy and Space Science, Chungnam National University, Daejeon 34134, Republic of Korea*

<sup>4</sup>*Instituto de Astrofísica de Canarias (IAC), E-38200 La Laguna, Tenerife, Spain*

<sup>5</sup>*Departamento de Astrofísica, Universidad de La Laguna (ULL), E-38206 La Laguna, Tenerife, Spain*

Submitted to the AAS Journals

## ABSTRACT

We continue our series of papers on phase-space distributions of stars in the Milky Way based on photometrically derived metallicities and Gaia astrometry, with a focus on the halo-disk interface in the local volume. To exploit various photometric databases, we develop a method of empirically calibrating synthetic stellar spectra based on a comparison with observations of stellar sequences and individual stars in SDSS, SMSS, and PS1, overcoming band-specific corrections employed in our previous work. In addition, photometric zero-point corrections are derived to provide an internally consistent photometric system with a spatially uniform metallicity zero point. Based on our phase-space diagrams, we find a strikingly narrow sequence in the rotational velocity ( $v_\phi$ ) versus metallicity ( $[\text{Fe}/\text{H}]$ ) space for a sample of high proper-motion stars ( $> 25 \text{ mas yr}^{-1}$ ), which runs along the Gaia Sausage/Enceladus (GSE) and the Splash sub-structures, and is connected to the disk. Notably, a rapid increase of  $v_\phi$  from a nearly zero net rotation to  $200 \text{ km s}^{-1}$  within a narrow metallicity interval ( $-0.8 < [\text{Fe}/\text{H}] < -0.2$ ) suggests that these stars were formed on a short gas-depletion time scale. Based on measurements of a scale height and length, we argue that they are distinct from stars dynamically heated by mergers, and are the relics formed during the starburst when the young Milky Way encountered the gas-rich GSE merger. The chain of high proper-motion stars, which we dub the Galactic Starburst Sequence (GSS), provides evidence that the post-merger metal-enriched gas settled onto the disk.

**Keywords:** Unified Astronomy Thesaurus concepts: Milky Way Galaxy (1054); Milky Way stellar halo (1060); Milky Way dynamics (1051); Milky Way formation (1053); Milky Way evolution (1052); Stellar abundances (1577); Stellar populations (1622)

## 1. INTRODUCTION

Photometric survey databases are useful resources for studying stellar populations and structures of the Milky Way Galaxy. The size of spectroscopic samples has grown rapidly in recent years, but photometric surveys still cover a significantly larger volume of space and thereby can provide the least-biased sample of Galactic stars. Multi-band observations are particularly useful, since they can be used to constrain fundamental stellar parameters, such as effective temperature ( $T_{\text{eff}}$ ) and metallicity ( $[\text{Fe}/\text{H}]$ ), with sufficient accuracy. The overall shape of a spectral energy distribution as traced by multi-band photometry depends on  $T_{\text{eff}}$ , and ultra-violet

excess provides information about a star’s metallicity. Importantly, photometric data can be combined with all-sky, high-precision astrometry from Gaia, providing rich information on chemical and kinematical properties of stars, as we demonstrated in a series of papers (An & Beers 2020, 2021a,b, hereafter Paper I, II, and III, respectively).

To obtain a clear view of Galactic stellar populations, one needs to establish accurate relationships between photometry and fundamental stellar parameters on an empirical basis or by using theoretical predictions. To take advantage of each method, we adopted a hybrid approach in previous papers in this series to cal-

ibrate theoretical isochrones of the main sequence using observations of well-studied Galactic globular and open clusters. The models were taken from YREC (Sills et al. 2000), and were combined with MARCS (Gustafsson et al. 2008) synthetic spectra, in order to convert  $T_{\text{eff}}$  and luminosities into photometric colors and magnitudes. Differences of the models from observations typically amount to a few hundredths of a magnitude for warm ( $T_{\text{eff}} > 5000$  K) stars, but they become as large as a few tenths of a magnitude for cooler stars. The model offsets are also a function of metallicity, in that more metal-rich cluster sequences tend to exhibit larger color deviations.

The observed offsets from the models are systematic in nature and cannot be simply reconciled by adjusting input cluster parameters, which implies that they may originate from errors in the input physics and physical parameters. To overcome these difficulties, we took the observed offsets as empirical correction factors that one needs to apply to our specific choice of theoretical stellar models. When models are used with empirical corrections, we obtain distances from SDSS photometry that are consistent with Gaia parallaxes, and our photometrically derived metallicities ( $[\text{Fe}/\text{H}]$ ) are also in overall agreement with spectroscopic measurements in SDSS (Paper I).

While we developed a method of deriving photometric metallicities from SDSS, this set of color- $T_{\text{eff}}$  corrections is only valid for observations taken in the SDSS *ugriz* filter set. Other photometric surveys also adopt filter sets similar to that of SDSS, but their transmission curves are not exactly the same as each other, leading to non-negligible differences in magnitudes. In this sense, direct calibration of synthetic spectra can serve as an alternative way of establishing such relations in various filter passbands. Importantly, it enables us to combine various photometric survey databases and produce chemokinematical phase-space maps over the entire celestial hemisphere in an internally consistent manner.

One of the goals in this study is to generalize our empirical-correction procedure, and construct a set of corrected synthetic spectra in order to generate magnitudes in any given filter set with high confidence. An essential requirement to achieve this goal is to finely sample flux for a set of calibration stars over a wide range of wavelength and stellar parameters using multi-band photometry, which has become practical in the era of massive photometric surveys. The basic idea of calibrating model fluxes in theoretical stellar spectra, as opposed to making corrections on individual color indices in the models, was introduced by Lejeune et al. (1997, 1998). However, the current work is based on

a significantly larger set of photometric, spectroscopic, and astrometric data, which were unavailable then.

The other goal of this work is to probe multi-dimensional data cubes constructed based on the revised metallicity estimates. In addition to chemical information from photometry, we exploit kinematic data from Gaia, as in the previous papers of this series. The majority of main-sequence stars in our sample are too faint to have radial velocity measurements. However, along the great circle perpendicular to the direction of disk rotation ( $l = 0^\circ$  and  $180^\circ$ ), rotational velocities ( $v_\phi$ ) in the cylindrical coordinate in the rest frame of the Galaxy do not depend on radial velocity. This enables to derive  $v_\phi$  by utilizing the proper motions of stars near the Galactic prime meridian and construct phase-space diagrams in  $v_\phi$  and  $[\text{Fe}/\text{H}]$ , which can subsequently be used to characterize kinematical and chemical properties of individual populations.

Because our method relies on calibration of theoretical models for main-sequence stars, our current approach is effectively limited to a local volume ( $d < 6$  kpc). Nonetheless, in our previous papers, we demonstrated the usefulness of such data by providing an unbiased, global perspective on local stellar populations, including Gaia Sausage/Enceladus (GSE; Belokurov et al. 2018; Helmi et al. 2018) and the Splash (Belokurov et al. 2020). In particular, we applied Gaussian mixture models in Paper III to isolate individual stellar populations, and evaluated their fractional contributions as a function of distance from the Galactic plane ( $Z$ ) and Galactocentric distance ( $R_{\text{GC}}$ ). In this work, we present evidence for yet another stellar population, which appears to have been formed during a starburst episode in the early evolution of the Galaxy, possibly induced by the GSE merger.

This paper is organized into two parts, which describe each of the above two subjects: the revised calibration of theoretical models (§ 2) and its application to photometric databases (§ 3). We summarize our results in § 4.

## 2. SPECTRUM-BASED EMPIRICAL CORRECTIONS ON THEORETICAL MODELS

Stellar metallicities presented in this study are computed using a set of theoretical stellar isochrones with revised empirical corrections. As described below, our new color- $T_{\text{eff}}$ - $[\text{Fe}/\text{H}]$  relations, which convert theoretically predicted quantities ( $T_{\text{eff}}$  and luminosity) into observables (colors and magnitudes), hinge on both stellar sequences and field stars with spectroscopic metallicity estimates; see An et al. (2009, 2013), Papers I and II, and references therein, for more information on

our previous model corrections. The same set of base theoretical models (Sills et al. 2000; Gustafsson et al. 2008) with identical model parameters, including an age-metallicity relation and  $\alpha$ -element abundance mixtures, are adopted in this work. In contrast to the models adopted in the previous papers of this series, this newer version of calibration utilizes photometry in various filter passbands over a wide range of wavelength, and thereby enables fine-tuning of synthetic stellar spectra.

### 2.1. Calibration Samples

As summarized in Table 1, we adopt both cluster sequences and a set of individual stars with spectroscopic metallicity estimates for the calibration of models. As shown in the first two columns, a total 19 passbands from various photometric surveys are utilized in this study: *ugriz* photometry from the Sloan Digital Sky Survey (SDSS) DR14, *uvgriz* from the SkyMapper Sky Survey (SMSS) DR2 (Onken et al. 2019), *grizy* from the Pan-STARRS1 surveys (PS1, Chambers et al. 2016), and *BV* from the AAVSO Photometric All-Sky Survey (APASS) DR10 (Henden et al. 2018). The *gri* photometry in APASS is not used owing to large photometric zero-point offsets (see also Tonry et al. 2018). We add to the list standard-star photometry in *BV<sub>IC</sub>* constructed by P. Stetson (see Stetson 2000).<sup>1</sup> Some of these databases use the same notation for their filter passbands (*ugriz*), but their response functions are not identical. Below we make a distinction between these filters by specifying the survey names.

Table 2 lists the stellar sequences adopted in this study. As in our previous exercise, we employ a set of well-studied Galactic globular and open clusters (M15, M92, M13, M3, M5, M67, and NGC 6791) over a wide range of metallicity ( $-2.4 \leq [\text{Fe}/\text{H}] \leq 0.4$ ). We use fiducial sequences from An et al. (2008), which were derived from the SDSS imaging data. Zero-point corrections (An et al. 2013) are applied to tie An et al. cluster photometry to SDSS DR14 (Abolfathi et al. 2018). Fiducial sequences in PS1 for the same set of clusters are taken from Bernard et al. (2014). For Stetson’s photometry, we only take data in *BV<sub>IC</sub>*, since the *U*-band and *R*-band are less well-defined than the others. At the time of this writing, cluster photometry in the SMSS and APASS filter systems is not yet available. In future work, we plan to improve the calibration of synthetic spectra by incorporating such data whenever they become available.

In addition to clusters, we employ the Gaia double sequence, which appears on a color-magnitude diagram from stars with large proper motions (Gaia Collaboration et al. 2018a). As demonstrated in Paper II, each of the sequences represents two dominant populations in the local halo – GSE and Splash – and has  $[\text{Fe}/\text{H}] \approx -1.3$  and  $-0.4$ , respectively (see also Sahlholdt et al. 2019). This dynamically defined group of stars also provides a powerful constraint on the shape of a sequence, bridging the gap between globular and open clusters at intermediate metallicities. We follow the procedure developed in Paper II to extract individual sequences from the Gaia double sequence (see Appendix A). In short, this technique relies on metallicity-sensitive *u*-band photometry to separate the two chemically distinct populations. For SDSS and SMSS, we use their *u*-band data. For PS1 and APASS, we use SDSS *u*. Additional cuts on kinematics further help to isolate each of the populations. As in our previous work, we compute  $v_\phi$  using Gaia’s proper motions and parallaxes, but without radial velocity measurements, within  $\pm 30^\circ$  along the Galactic prime meridian. To construct a clean sequence, we use objects with good astrometry, having less than 20% uncertainty in parallax and 30% uncertainty in proper motion. We also apply cuts on  $E(B - V) < 0.1$  and  $|b| > 20^\circ$ . As in Paper II, we impose  $-150 < v_\phi \leq -50 \text{ km s}^{-1}$  and  $120 < v_\phi \leq 150 \text{ km s}^{-1}$  on the sample to derive the blue (metal-poor) and red (metal-rich) main sequences, respectively, for which we compute weighted median colors in bins of 0.5 mag in  $M_r$  ( $\Delta M_r = 0.2 \text{ mag}$  in  $u - r$  CMDs).

For individual calibration stars with spectroscopic metallicities, we utilize the Sloan Extension for Galactic Understanding and Exploration (SEGUE, Yanny et al. 2009; Rockosi et al. 2022) and the Galactic Archaeology with HERMES (GALAH) survey (Buder et al. 2021), as they are among the largest and most uniform spectroscopic data sets in the Northern and Southern Hemisphere, respectively. Specifically, we adopt metallicity estimates from a rerun of the updated SEGUE Stellar Parameter Pipeline (SSPP; Lee et al. 2008a,b), performed by one of the coauthors (Y. S. Lee). We apply cuts based on a signal-to-noise ratio (SNR) of the spectra ( $> 30$ ), uncertainty in  $T_{\text{eff}} < 200 \text{ K}$ , and  $\log g > 3.5$  to select main-sequence stars with high-quality parameter estimates. For the GALAH sample, we also require that a stellar parameter quality flag (`flag_sp`) and an overall iron abundance quality flag (`flag_fe_h`) are not set.

The advantage of the SEGUE and GALAH samples is corroborated by the availability of photometric data in

<sup>1</sup> <https://www.canfar.net/storage/list/STETSON/Standards>.

**Table 1.** A Summary of Calibration Samples

Photometry	Bandpasses	Stellar sequences	Individual stars (spectroscopic sample)
SDSS	<i>ugriz</i>	An et al. (2008), Gaia double	SEGUE, GALAH
SMSS	<i>uvgriz</i>	Gaia double	SEGUE, GALAH
PS1	<i>grizy</i>	Bernard et al. (2014), Gaia double	SEGUE, GALAH
APASS	<i>BV</i>	Gaia double	SEGUE, GALAH
Stetson	<i>BV<sub>I</sub>C</i>	Stetson’s standard photometry	...

**Table 2.** Fundamental Parameters and Uncertainties of Stellar Sequences

Cluster/Sequence	[Fe/H] <sup>a</sup>	( <i>m</i> − <i>M</i> ) <sub>0</sub> <sup>a</sup>	<i>E</i> ( <i>B</i> − <i>V</i> ) <sup>a</sup>	age <sup>a</sup>	Min <i>M<sub>r</sub></i> <sup>b</sup>	References <sup>c</sup>
Name	(dex)	(mag)	(mag)	(Gyr)	(mag)	
M15	−2.42 ± 0.10	15.25 ± 0.15	0.100 ± 0.020	13.0 ± 2.6	19.4	1/1/1
M92	−2.38 ± 0.10	14.64 ± 0.15	0.020 ± 0.004	13.0 ± 2.6	18.5	1/2/1
M13	−1.60 ± 0.10	14.38 ± 0.15	0.020 ± 0.004	13.0 ± 2.6	18.5	1/2/1
M3	−1.50 ± 0.10	15.02 ± 0.15	0.010 ± 0.002	13.0 ± 2.6	19.0	1/1/1
Gaia double (blue MS)	−1.30 ± 0.10	... <sup>d</sup>	... <sup>d</sup>	13.0 ± 2.6	4.0	3/./.
M5	−1.26 ± 0.10	14.46 ± 0.15	0.030 ± 0.006	12.0 ± 2.4	18.5	1/2/1
Gaia double (red MS)	−0.40 ± 0.10	... <sup>d</sup>	... <sup>d</sup>	12.0 ± 2.4	4.0	3/./.
M67	+0.00 ± 0.01	9.61 ± 0.03	0.041 ± 0.004	4.0 ± 0.5	13.0	4/4/4
NGC 6791	+0.37 ± 0.07	13.06 ± 0.06	0.120 ± 0.020	9.0 ± 1.0	17.6	4/4/4

<sup>a</sup>Uniform uncertainties except for M67 and NGC 6791.

<sup>b</sup>A minimum *M<sub>r</sub>* to select MS stars.

<sup>c</sup>References for [Fe/H], (*m* − *M*)<sub>0</sub>, and *E*(*B* − *V*), respectively: (1) Kraft & Ivans (2003); (2) Carretta et al. (2000); (3) Paper II; (4) An et al. (2019) and references therein.

<sup>d</sup>Parallaxes for individual field stars in Gaia EDR3, along with their foreground extinctions in Schlegel et al. (1998).

various passbands (such as SMSS *uv*; see Table 1), while a stable baseline provided by the cluster sample makes the sequence-based approach reliable. All SEGUE stars are covered by SDSS and PS1 imaging surveys, but can only be matched to objects in SMSS near the equatorial region. Likewise, the majority of GALAH stars have good matches to SMSS photometry, but only a small fraction of its survey area overlaps with SDSS. Primary stellar sources (`type`= 6) in the SDSS are kept, with a set of minimal quality flags in the *r*-band measurements to ensure that sources do not have issues such as de-blending, interpolation, and saturation. Similarly, primary detections in PS1 from its stacked imaging catalog are taken. We select point-like sources by imposing a maximum 0.05 mag difference in *i*-band photometry between a point-spread function and Kron magnitudes. For SMSS, we apply cuts on a number of photometric

quality flags to only retain good photometric measurements: `class_star` > 0.9, `flags` < 3, `nch_max` = 1, `prox` > 7.5, `ngood_min` > 1, and `nimaflags` = 0 in each passband.

Photometric catalog objects are matched with Gaia Early Data Release 3 (EDR3, Gaia Collaboration et al. 2021) and Data Release 3 (DR3, Gaia Collaboration et al. 2022) using a 1'' search radius. Zero-point corrections on parallax by the Gaia team (Lindgren et al. 2021) are adopted. In the following calibration, objects with good parallaxes ( $\sigma_\pi/\pi < 0.2$ ) are used; about 68 % of them have parallaxes within 2% from those inferred based on Bayes’ theorem (Bailer-Jones et al. 2021). The foreground reddening values in Schlegel et al. (1998) are adopted, except for clusters, along with extinction coefficients at  $R_V = 3.1$  in Schlafly & Finkbeiner (2011) for SDSS,

PS1, and Johnson-Cousins (those listed as ‘Landolt’) bands. For SMSS, we adopt values in Wolf et al. (2018). These coefficients assume 14% reduction in the original  $E(B - V)$  in Schlegel et al. (1998).

## 2.2. Spectrum-based Corrections

### 2.2.1. Scope

Because the overall shape of a spectrum is influenced by  $T_{\text{eff}}$  and metallicity, and by  $\log g$  to a lesser degree, we aim to provide an empirically calibrated set of synthetic stellar spectra over a wide range of  $T_{\text{eff}}$  and  $[\text{Fe}/\text{H}]$ , which in turn can be employed to derive such quantities in other stars. For this purpose, theoretical flux ratios between different filter passbands (color indices) are computed as a function of wavelength, and any deviation from the calibration data are attributed to systematic errors in the models. All flux ratios are referenced to the SDSS or SMSS  $r$ -band among different filter passbands, because of the large amount of flux collected in this passband, and its relatively weak metallicity sensitivity in the  $T_{\text{eff}}$  regime considered in this study ( $4000 < T_{\text{eff}} < 7000$  K). Its bolometric corrections are also less prone to systematic errors.

We derive synthetic stellar colors from MARCS model atmospheres (Gustafsson et al. 2008); see An et al. (2009) for more information on the construction of the MARCS model library. Filter-response curves in SDSS  $ugriz$  are found on the project webpage.<sup>2</sup> References for other filter transmissions are Tonry et al. (2012, PS1 *grizy*), Bessell et al. (2011, SMSS *uvgriz*), and Bessell & Murphy (2012, Johnson-Cousins  $BVI_C$ ). APASS  $BV$  are taken from the SVO filter profile service.<sup>3</sup> When deriving a Vega magnitude, we use a Vega model from the HST CALSPEC library (Bohlin et al. 2014), with the suggested flux re-scaling from Riello et al. (2021). Effective wavelengths ( $\lambda_{\text{eff}}$ ) of the filter passbands are computed for each model, as they have a mild dependence on the underlying stellar spectrum (primarily on  $T_{\text{eff}}$ ).

Isochrones generated using YREC (Sills et al. 2000) are combined with MARCS synthetic colors. For a given  $[\text{Fe}/\text{H}]$ , differences in colors between observational data and models are computed as a function of absolute magnitude in the  $r$ -band ( $M_r$ ). We use  $M_r$  to infer  $T_{\text{eff}}$  from a  $M_r$ - $T_{\text{eff}}$  relation in the isochrones, because spectroscopic  $T_{\text{eff}}$  measurements are not typically available for individual stars in a stellar sequence. The infrared flux method (IRFM) is another useful way of deriving

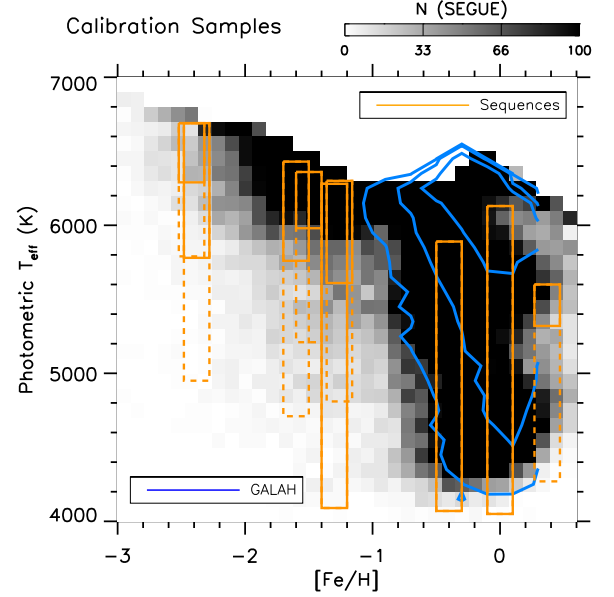


**Figure 1.** The  $T_{\text{eff}}$ - $[\text{Fe}/\text{H}]$  space covered by the calibration sample. The orange solid rectangles exhibit main sequences of clusters and the Gaia double sequence with  $u$ -band measurements in SDSS, while more extended sequences with deeper  $gr$  photometry are shown by orange-dashed lines. The number density of SEGUE and GALAH stars is shown by the gray histogram and blue contours, respectively. Only those having  $\text{SNR} > 30$ ,  $\log g > 3.5$ , and photometric  $T_{\text{eff}}$  errors less than 200 K are retained for these individual spectroscopic metallicity measurements.

$T_{\text{eff}}$  from photometry, but our approach makes a specific prediction on both  $T_{\text{eff}}$  and  $\log g$  of a star, which are necessary ingredients for generating precise synthetic model colors. There also exist  $T_{\text{eff}}$  scale differences of a few hundred kelvin between photometric and spectroscopic approaches (e.g., Pinsonneault et al. 2004). For this reason, instead of taking spectroscopic  $T_{\text{eff}}$ , we compute  $T_{\text{eff}}$  photometrically using stellar isochrones in the same manner as for the stellar sequences. This significantly reduces systematic differences in color- $T_{\text{eff}}$  relations from our heterogeneous data sets, and makes color- $T_{\text{eff}}$ - $[\text{Fe}/\text{H}]$  relations internally more consistent.

Figure 1 displays a  $T_{\text{eff}}$ - $[\text{Fe}/\text{H}]$  space covered by the stellar sequences and spectroscopic targets in our sample, where the  $T_{\text{eff}}$  are determined from our isochrones. Stellar sequences in SDSS are shown by orange boxes with a width of  $\pm 0.1$  dex in  $[\text{Fe}/\text{H}]$ . The dotted lines represent the same sequences, but without valid  $u$ -band measurements, demonstrating the necessity of deeper  $u$ -band photometry. Stellar sequences have discrete metallicities, while the spectroscopic sample (the gray-scale histogram for SEGUE and contours for GALAH targets) fills up the remaining space. Our spectroscopic sample is heavily weighted by metal-rich stars, with a significantly

<sup>2</sup> <https://www.sdss.org/instruments/camera/#Filters>

<sup>3</sup> <http://svo2.cab.inta-csic.es/svo/theory/fps3>



lower number in the metal-poor regime ( $[\text{Fe}/\text{H}] < -1$ ). The upper right side is not covered by both samples, owing to the increased metal content and relatively old ages of the stars. The lower left part is depopulated because of the lack of faint metal-poor main-sequence stars in the spectroscopic surveys.

### 2.2.2. Model Comparisons

For each star in the spectroscopic sample, an isochrone is generated by interpolating the model grid at the star’s metallicity ( $[\text{Fe}/\text{H}]$ ), and differences in flux are computed in various filter passbands, as done for the stellar sequences. However, to evenly sample cluster sequences and the spectroscopic targets, we bin each of the SEGUE and GALAH samples in  $[\text{Fe}/\text{H}]$  and compute *mean* flux offsets as a function of  $T_{\text{eff}}$  (see Appendix A). In accordance with the metallicity of the observed stellar sequences (Table 2), the central metallicities are set to  $[\text{Fe}/\text{H}] = \{-2.4, -1.6, -1.3, -0.4, 0.0, +0.3\}$ . To match this binning and keep the average metallicity of a subset of stars as close as possible to the central metallicity values, each spectroscopic sample is divided into  $[\text{Fe}/\text{H}] = \{(-2.9, -2.1), (-1.8, -1.4), (-1.5, -1.1), (-0.5, -0.3), (-0.1, 0.1), (+0.2, +0.4)\}$ . A large width (0.8 dex) is set in the lowest metallicity bin to compensate for the small number of stars in the sample. Because the flux difference from our models changes mildly with metallicity, our adopted bin sizes have little impact on the calibration. Nonetheless, mean flux offsets from GALAH are taken only at  $[\text{Fe}/\text{H}] = \{-0.4, 0.0, +0.3\}$  due to the lack of metal-poor stars in the sample.

Figures 2 and 3 show color differences in magnitude between models and observations, as a function of  $\lambda_{\text{eff}}$ , at two selected  $T_{\text{eff}}$  (5800 K and 4500 K, respectively). In each panel, differences are shown for the sequences and an ensemble of spectroscopic targets in open and filled symbols, respectively, and different symbols are used to indicate references for photometry. All flux differences are registered to the SDSS *r*-band, or the SMSS *r*-band for the GALAH sample, owing to a relatively small number of cross-matches with SDSS objects in the Southern sky. The differences from the model at these two *r* passbands are nearly the same, and are defined to be zero (i.e., their bolometric corrections are assumed to be correct).<sup>4</sup>

<sup>4</sup> Similarly, because cluster fiducial sequences in PS1 (Bernard et al. 2014) are not directly tied to SDSS photometry, color indices are registered using the PS1 *r*-band, instead of the fiducial SDSS *r*-band. Nevertheless, differences from model colors in the PS1 *r*-band are negligible (see Appendix A). Thus, the effect of switching between SDSS *r*-band and PS1 *r*-band is not significant.

Error bars for the stellar sequences in Figures 2 and 3 represent propagated uncertainties from photometry and input parameters ( $[\text{Fe}/\text{H}]$ ,  $(m - M)_0$ ,  $E(B - V)$ , and age; Table 2). For the fiducial sequences in SDSS and PS1, constant uncertainties of 0.02 mag are assumed in the color indices. Similarly, a 2% error is adopted for the mean colors of Stetson’s  $BVI_C$  cluster sequences as a conservative limit. Photometry of Gaia’s double sequence is collected across a large area on the sky, and therefore an observed scatter is taken as uncertainties in the mean colors, since it represents a sum of random and systematic zero-point errors, unless propagated photometric uncertainties are larger. A comparison of APASS photometry to Stetson’s standard photometry for the sample clusters (except NGC 6791) reveals an rms dispersion of 0.04 mag in *BV*. Thus, it is added in quadrature to a total error budget for the APASS-based double sequence.

For the spectroscopic sample, the error bars in Figures 2 and 3 also indicate the quadratic sum of random and systematic uncertainties. The random component includes uncertainties in photometry, spectroscopic  $[\text{Fe}/\text{H}]$ , and Gaia parallax. For the systematic uncertainty, a 0.1 dex in  $[\text{Fe}/\text{H}]$  is assumed to take into account a scale difference between our models and the spectroscopic determinations. A 20% uncertainty in age is adopted for all stars. Flux differences from these systematic uncertainties are typically less than 0.01 mag in *grizyBV*, but are as high as 0.05 mag in *uv* at high metallicities. In APASS, 0.04 mag uncertainty in photometry is further incorporated into the final uncertainty (see above).

In Figures 2 and 3, there are systematic differences between the two classes of samples. For instance, the stellar sequences tend to show smaller flux deviations from the models than the spectroscopic sample; at  $[\text{Fe}/\text{H}] \geq -0.4$ , our result indicates that the spectroscopic sample is fainter at  $\lambda < 4000 \text{ \AA}$ , but brighter at  $\lambda > 7000 \text{ \AA}$  than the sequences. Indeed, the cluster sequences in PS1 *grizy* (Bernard et al. 2014) exhibit the smallest differences overall. Such a difference can be caused by inconsistent metallicity scales, but other sources of errors, such as adopted ages, may also contribute to the observed offset, although the absolute model deviation changes monotonically with age, without modifying the observed wavelength-dependent offsets.

In Figures 2 and 3, the red line indicates an average model deviation as a function of  $\lambda_{\text{eff}}$ . Mean magnitude differences between models and observational data are computed by linearly interpolating values at three adjacent filter  $\lambda_{\text{eff}}$ . They are smoothed by applying a boxcar average with a width of 1000  $\text{\AA}$ , which is comparable to

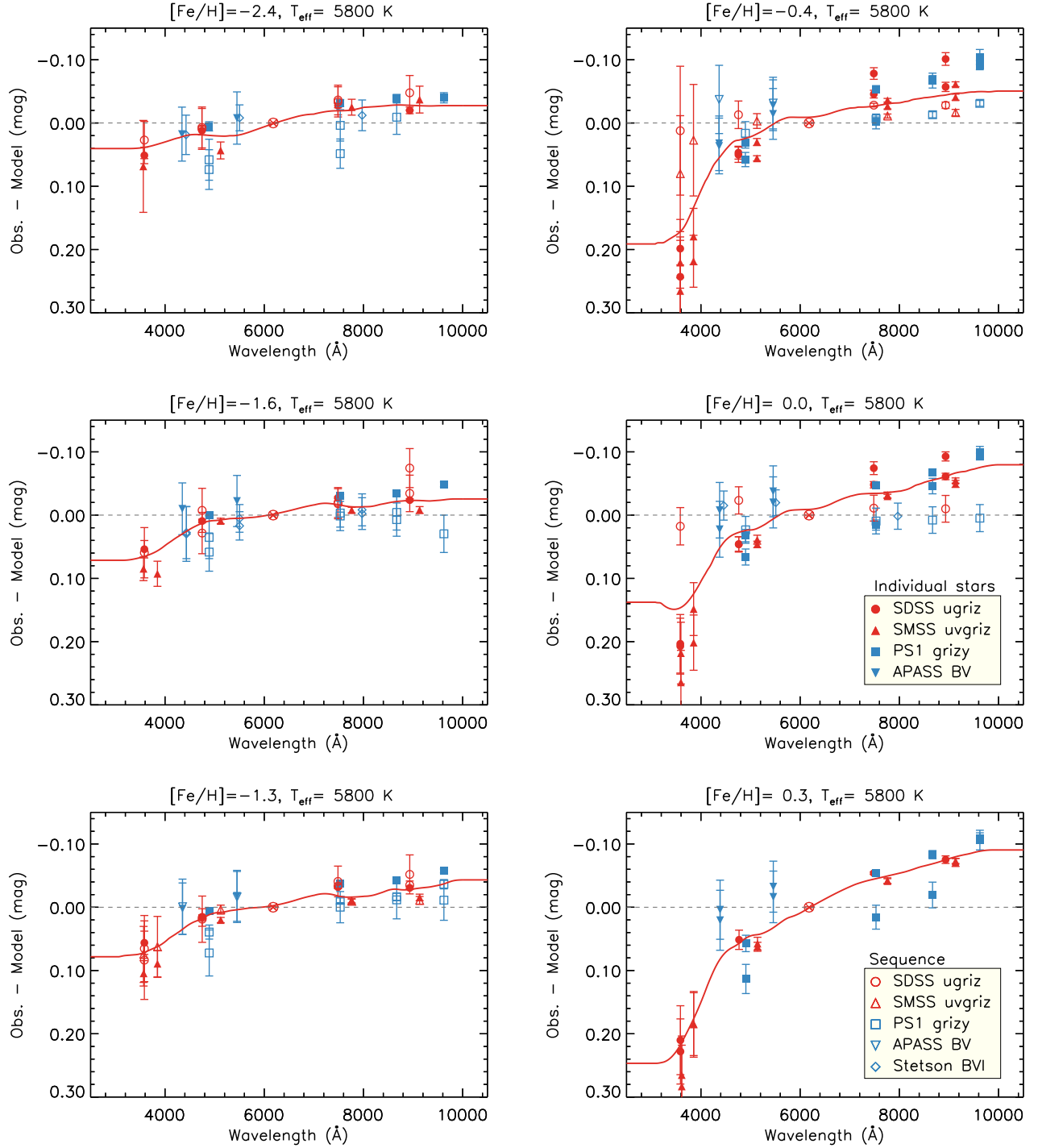


**Figure 2.** Magnitude differences between observed data and isochrones as a function of  $\lambda_{\text{eff}}$  of filter passbands. A  $T_{\text{eff}} = 5800$  K case is shown above to display the overall quality of a comparison based on stellar sequences (globular, open clusters, and Gaia’s double sequences; open symbols) and spectroscopic measurements of individual stars from SEGUE and GALAH (filled symbols). Comparisons are made in six metallicity bins at  $[\text{Fe}/\text{H}] = -2.4, -1.6, -1.3, -0.4, 0.0,$  and  $0.3$ , respectively (from top left to bottom right panels). The red solid line represents moving averages of the difference as a function of  $\lambda_{\text{eff}}$  (see text).

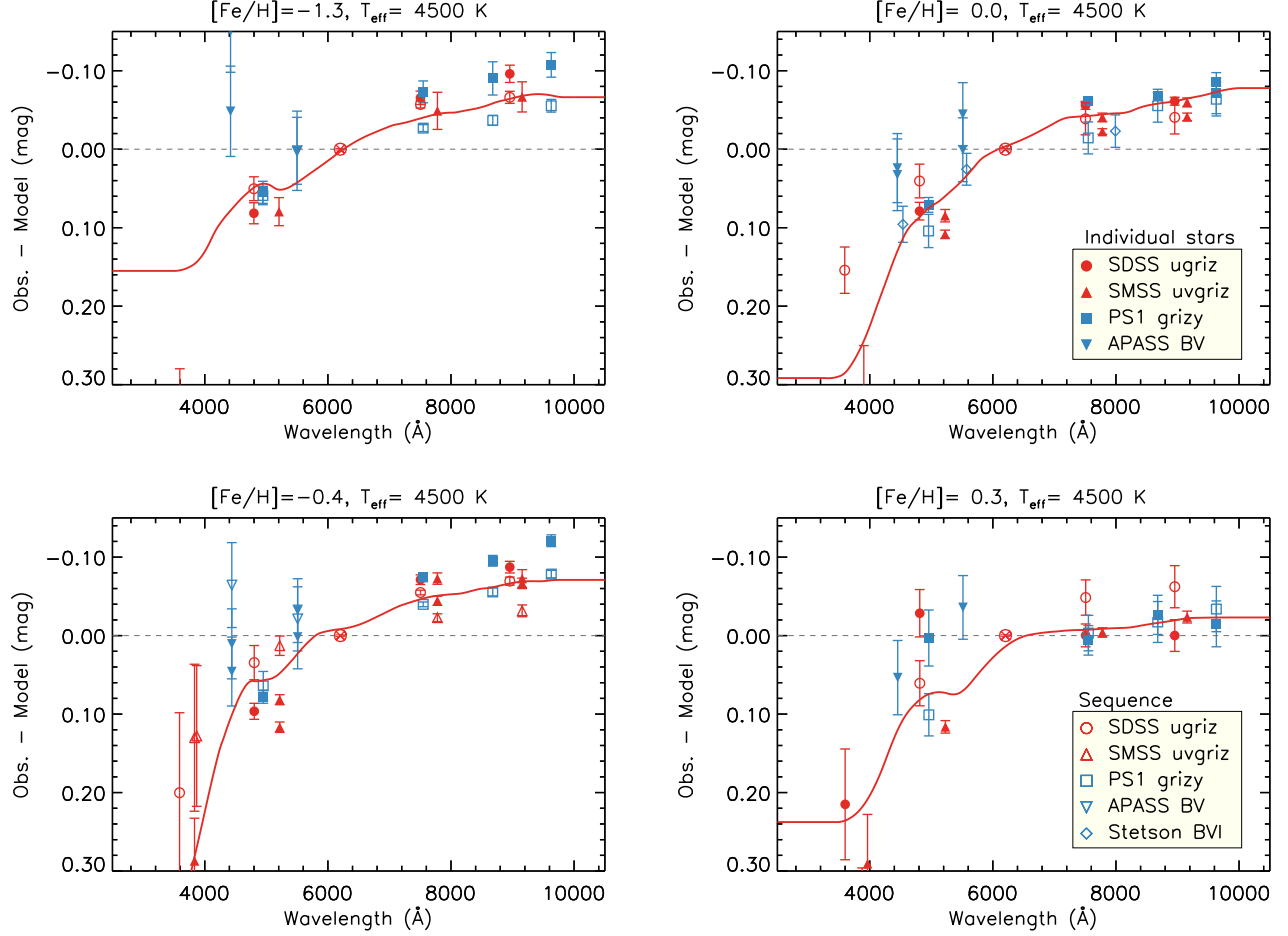


**Figure 3.** Same as in Figure 2, but at  $T_{\text{eff}} = 4500$  K. Comparisons in the two lowest metallicity bins are not shown due to the lack of observational data in this  $T_{\text{eff}}$  bin.



the FWHM of a broad filter passband. Average differences indicate that our models greatly over-estimate flux below 5000 Å, by up to 20%, while they under-estimate flux at longer wavelengths, by 10% at the most. The *BV* photometry from APASS (open and filled downward triangles) exhibits consistently larger fluxes than the other calibration sample by 0.05–0.1 mag, but the differences from the mean line are within our estimated  $1\sigma$  uncertainties. We suspect all-sky photometric zero-point errors (at roughly 4% levels) as a likely source of the systematics (see above).

### 2.2.3. Construction of a Correction Cube

Figure 4 displays model differences as a function of  $[\text{Fe}/\text{H}]$ . Each data point represents one of the metallicity groups in this work. As shown by the blue lines, a 3<sup>rd</sup>-order polynomial function is used to depict the observed trend. Beyond the metallicity range covered by the sample, a constant offset is assumed in the model deviation. Figure 5 displays slices of these mean model deviations at some selected wavelengths. Red colors indicate that models over-predict the flux, while the blue colors show regions with under-predicted flux. In this way, we construct a three-dimensional data cube of model deviations as a function of  $T_{\text{eff}}$ ,  $[\text{Fe}/\text{H}]$ , and wavelength.

To first order, the model deviations change monotonically with wavelength: models are brighter than observations at shorter wavelengths, while the sign reverses at longer wavelengths. This suggests an offset in the  $T_{\text{eff}}$  scale of the isochrones as a major source of the systematic mismatch. However, the required amount of offset must be very large, by about 400 K, even for warm stars (Figure 6); it is even larger for cooler stars. Even if there are systematic differences between different approaches of determining  $T_{\text{eff}}$ , such as the IRFM and spectroscopic determination from excitation/ionization balance, this is beyond the accepted range of errors in the models. Therefore, it seems that the observed offsets originate from a combination of various sources of systematic errors, such as incorrect input physics or under-estimated line absorption in the models. Boundary conditions in stellar-interior models may also be incompatible with the atmosphere models in this study. On the observational side, an inconsistent metallicity scale, incorrect assumptions on elemental-abundance ratios, or errors in the assumed age could be responsible for the systematic  $T_{\text{eff}}$  offsets.

The model differences are highly non-linear in the  $[\text{Fe}/\text{H}]$  versus  $T_{\text{eff}}$  space, and no simple correction of the theoretical isochrones is possible to remedy the problem. For this reason, we take the observed flux offsets in Figure 5 as a correction matrix for our choice

of stellar isochrones and synthetic spectra. More specifically, we employ a semi-empirical approach to correct synthetic spectra based on observations, while keeping stellar-interior models intact. Unlike in our previous work, the data cube in Figure 5 provides a continuous function of magnitude correction in wavelength. Thus, the corrected synthetic spectra can be applied to any filter sets in the wavelength range covered by our calibration sample.

### 2.2.4. Comparison with Previous Calibration

In comparison to purely theoretical models, the net result of our empirical corrections is redder colors or a higher photometric  $T_{\text{eff}}$ , due to over-estimation of the model flux at shorter wavelengths and under-estimation at longer wavelengths. Apart from this fundamental change in the models, the revised calibration also differs from our earlier versions of the empirical corrections. The biggest change is the inclusion of individual spectroscopic targets in the sample, which inevitably modifies the metallicity scale of the models. As shown earlier in Paper I, isochrones calibrated using fiducial clusters produce photometric metallicities that are in agreement with spectroscopic estimates in SEGUE within  $\Delta[\text{Fe}/\text{H}] \sim 0.1$  dex at  $[\text{Fe}/\text{H}] > -1.5$ , but the difference amounts to  $\sim 0.4$  dex at  $[\text{Fe}/\text{H}] = -2$ , in the sense of a lower metallicity from our cluster-based approach. Such a difference is a direct consequence of a systematic offset in the metallicity scale between the cluster sequences and the SEGUE stars.

Figure 7 compares the photometric metallicities from Paper III with those in this work, based on the revised calibration. The comparisons are shown for the solutions based on Gaia parallaxes using SDSS *ugriz* photometry. Only stars having distance uncertainties less than 10% and  $E(B - V) < 0.1$  are included. Other constraints are the same as for the main sample, as described in the next section, except in the top panel, which displays a metallicity difference over the full range of  $M_r$ . The large deviations for bright stars are evident, which are caused by the lack of hot stars in the calibration sample (Figure 1). In our subsequent analysis, including the bottom panel of Figure 7, we adopt  $4.5 < M_r < 7.5$  to avoid regions with potentially large calibration errors.

The weighted median difference in Figure 7 indicates that the two calibration versions agree at high metallicity ( $[\text{Fe}/\text{H}] > -1$ ), but that photometric metallicities from this work become larger for metal-poor stars, amounting to 0.35 dex at  $[\text{Fe}/\text{H}] = -2$ . Because the GALAH sample is confined to metal-rich stars in our calibration, the systematic trend highlights an inconsistent match of the metallicity scales between the clus-

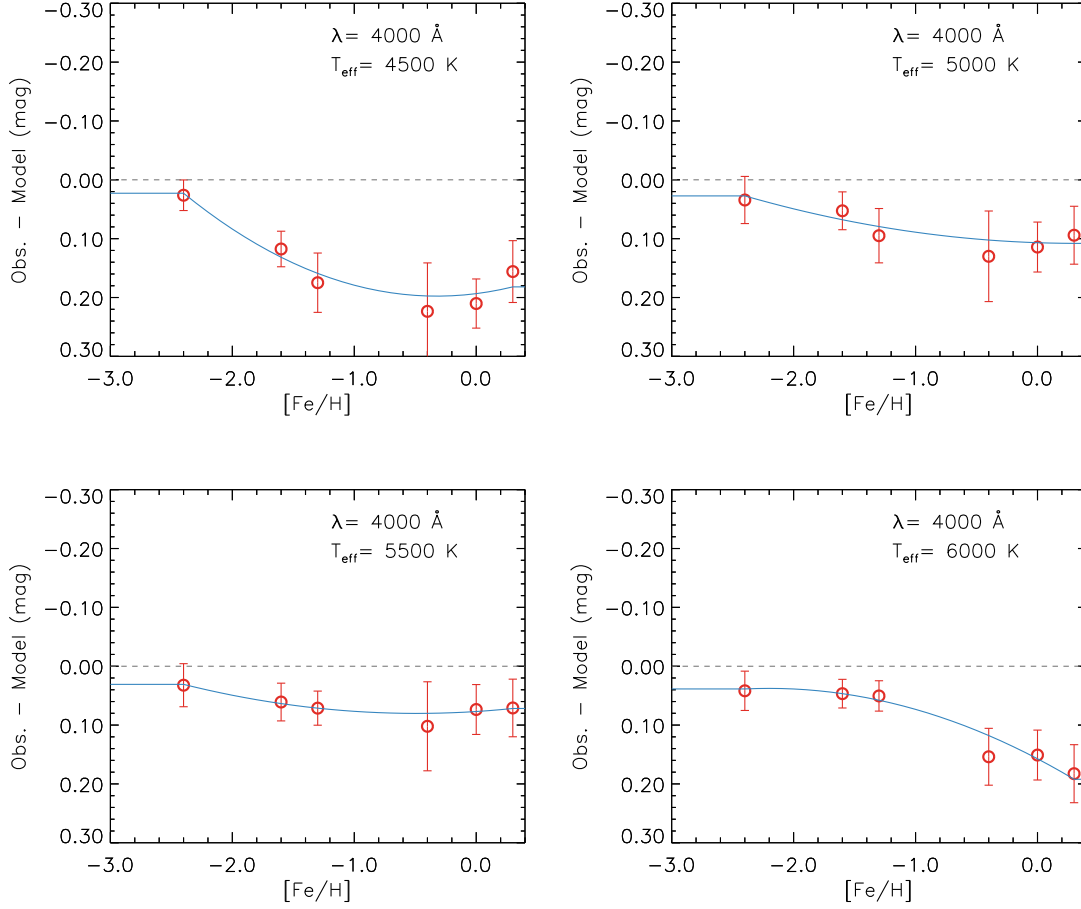


**Figure 4.** Mean magnitude differences at  $\lambda = 4000 \text{ \AA}$ , as a function of  $[\text{Fe}/\text{H}]$ , at selected  $T_{\text{eff}}$ . Each point represents one of the metallicity groups in this work. The blue line represents the best-fitting 3rd-order polynomial. Constant offsets are assumed beyond the metallicity range covered by the data.

ter sequences and SEGUE stars. The SSPP estimates have been checked thoroughly using clusters and high-resolution spectroscopic abundance determinations, and the overall agreement is impressive (Rockosi et al. 2022). Nonetheless, such comparisons are biased to giants and main-sequence turn-off stars in the metal-poor regime, due to the lack of metal-poor main-sequence dwarfs in the SEGUE sample with a sufficiently high SNR. Therefore, the difference may originate from an internally inconsistent metallicity scale between dwarfs and giants in the SEGUE sample.

In summary, because neither metallicity scale is preferred over the other, the revised isochrones obtained in the current experiment should be taken as an alternative to our earlier cluster-based calibration. More precisely, a metallicity distribution of metal-poor stars obtained in this study based on the hybrid sample is hinged on an intermediate metallicity scale between SEGUE and the cluster-based work, set by their relative weights to the

final calibration sample. The sense is that it is skewed toward more metal-rich stars below  $[\text{Fe}/\text{H}] = -1$  compared to previous work of this series.

### 3. CHEMO-KINEMATICAL PROPERTIES OF THE LOCAL HALO

In this section, we apply our newly calibrated set of models to large photometric catalogs, and provide new insights for Galactic stellar populations in the local volume. In addition to chemical information from photometry, we exploit kinematical data from Gaia to generate phase-space maps at various distances from the Galactic plane and Galactocentric distances. As in our previous papers, we restrict our analysis to a strip within  $\pm 30^\circ$  from the Galactic prime meridian ( $l = 0^\circ$  and  $180^\circ$ ), where a conversion from transverse motions into  $v_\phi$  is reliable (see Paper III for more details). Below, we first inspect metallicity distributions and phase-space diagrams to validate our new calibration (§ 3.1), and present distributions of scale heights and lengths for each group of

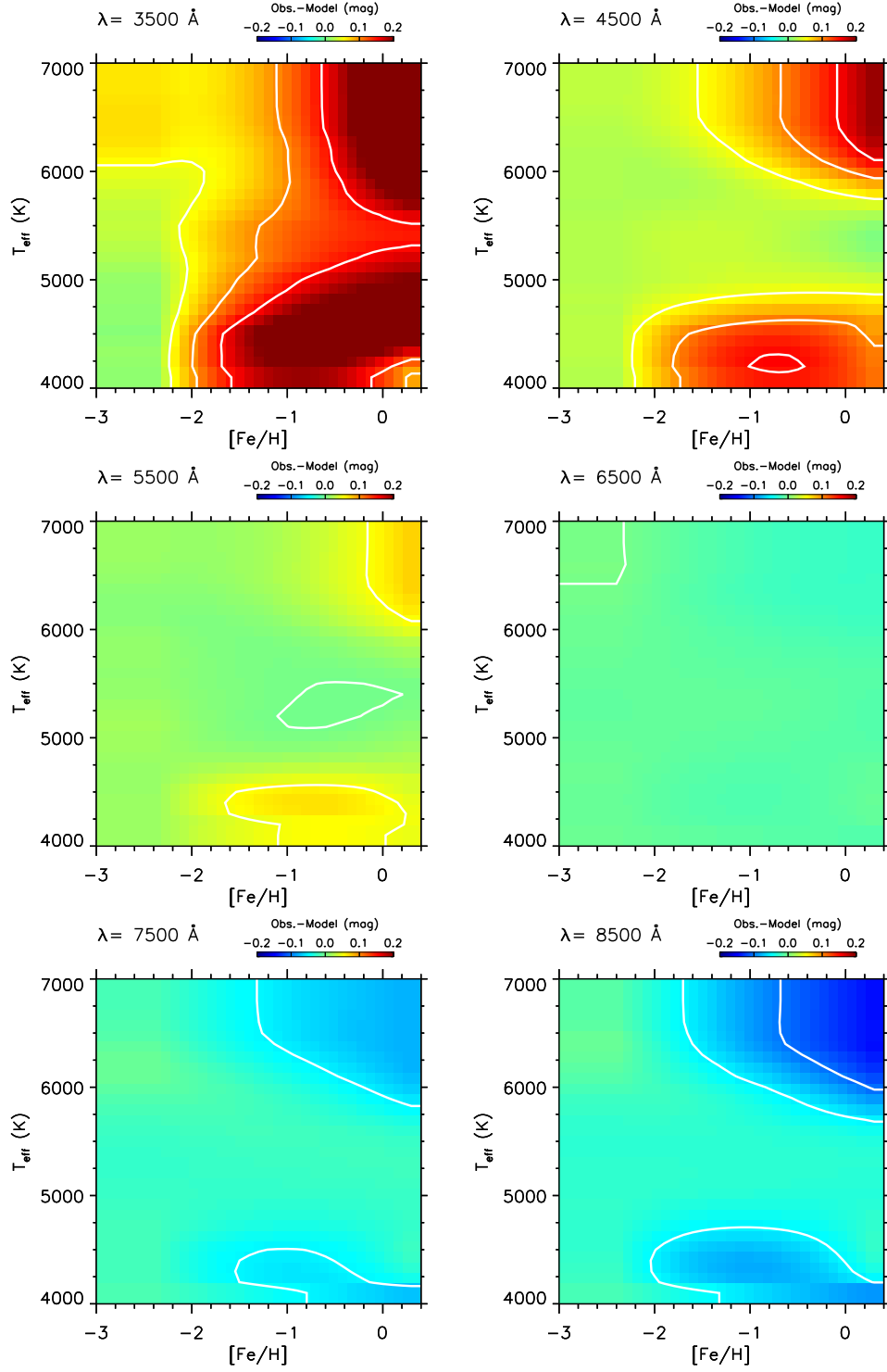


**Figure 5.** Mean magnitude offsets of the original models from observational data in  $[\text{Fe}/\text{H}]$  versus  $T_{\text{eff}}$  at selected wavelengths.

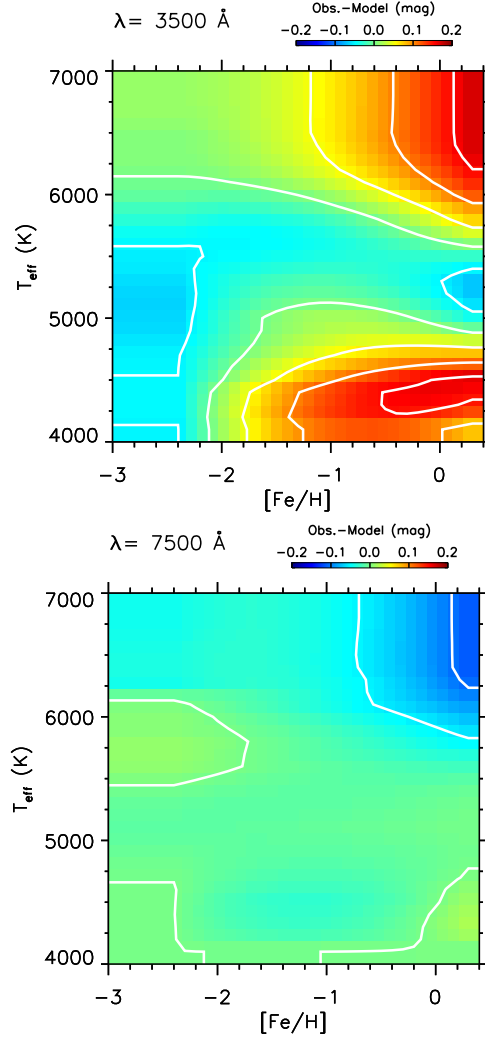


**Figure 6.** Same as in Figure 5, but assuming 400 K cooler  $T_{\text{eff}}$  in the YREC isochrones.

stars in bins of  $v_\phi$  and  $[\text{Fe}/\text{H}]$  (§ 3.2). Based on phase-space diagrams of high proper motion stars, we demonstrate that our data reveal yet another stellar population formed during a period of Galactic starburst activity (§ 3.3).

### 3.1. Validation of Photometric Metallicity Estimates

In the following applications, we use Gaia EDR3 as a main source catalog, since  $v_\phi$  in the rest frame of the Galaxy is a major ingredient of our phase-space diagrams. We combine Gaia EDR3 astrometric data with photometry in SDSS, SMSS, and PS1 using a  $1''$  match radius. As there is a little overlap between SDSS and SMSS, two combined catalogs —  $\text{SDSS} \cap \text{Gaia}$  and  $\text{SMSS} \cap \text{Gaia}$ , respectively — are created, in addition to a master photometric catalog from all survey data. PS1 *grizy* photometry is added to each data set, when there

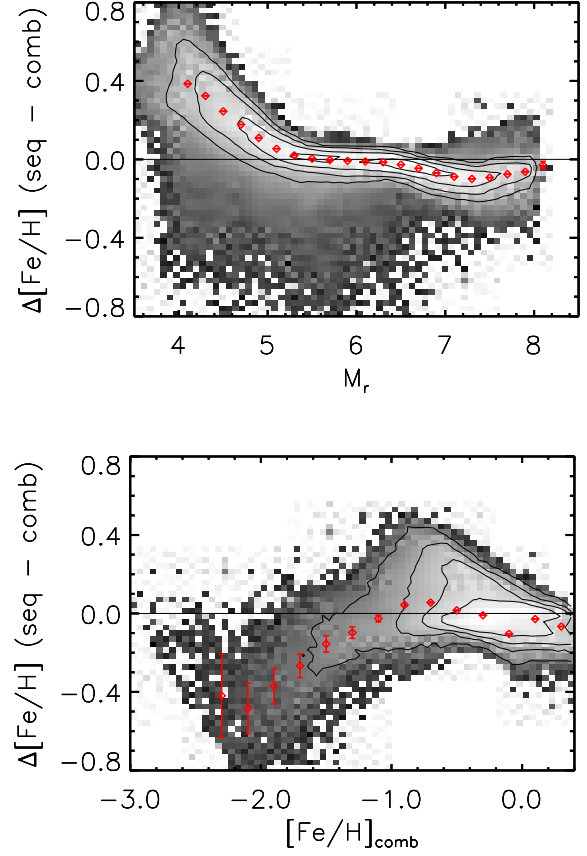


**Figure 7.** Comparison between photometric metallicity estimates using calibrated models in Paper III (‘seq’: sequence-based) and this work (‘comb’: combined from both cluster sequences and spectroscopic samples). A logarithmic number density is shown with arbitrary contour levels. The open diamonds show a weighted median difference in bins of  $\Delta M_r = 0.2$  and  $\Delta[\text{Fe}/\text{H}] = 0.2$  dex, respectively, with error bars indicating its uncertainty. Only those having  $\sigma_\pi/\pi < 0.1$  and  $E(B - V) < 0.1$  are included in the above comparisons. The comparison in the bottom panel is further restricted to  $4.5 < M_r < 7.5$ .

exist SDSS or SMSS photometry, to better constrain the stellar parameters.

For each set of catalogs, we estimate metallicities for individual stars through a grid search of calibrated models, imposing Gaia parallaxes in this computation. For the uncertainty in metallicity, we propagate parallax uncertainties by assuming  $1\sigma$  lower/higher parallaxes and taking differences in the metallicity estimation. The final uncertainties in metallicity are a quadratic sum of this propagated uncertainty and the one from a  $\Delta\chi^2 = 2.3$  boundary for two degrees of freedom. Only solutions showing at minimum fair model matches (judged from a reduced  $\chi^2$  of the fit less than 3 and detected in at least five photometric passbands) are kept. See Paper I for

detailed information on model comparisons and quality cuts on the sample.

Figure 8 shows metallicity maps of stars in the local volume ( $1.2 < d < 3$  kpc) in the Galactic coordinate system (Mollweide projection), based on our metallicity estimates for individual stars in each of the three combined catalogs. Panel (a) displays a map from SDSS  $\cap$  Gaia, which mostly covers the Northern Galactic Hemisphere, while panel (b) shows the Southern Hemisphere from SMSS  $\cap$  Gaia. Panel (c) displays a full coverage map from SDSS, SMSS, and PS1. All three maps are smoothed using a median filter with a  $2^\circ$  radius. There are some overlaps between SDSS  $\cap$  Gaia and SMSS  $\cap$  Gaia, mainly along the celestial equator, but they are not significant overall. For the same reason, a weak discontinuity appears in the overlapping areas. Low latitude regions ( $|b| < 20^\circ$ ) and some areas are excluded to avoid large cumulative extinction,  $E(B - V) > 0.1$ , which would otherwise affect our photometric parameter estimates.

Reassuringly, Figure 8 reveals that more metal-rich stars are found near the Galactic plane, from which a mean metallicity gradient is evident from the low to high Galactic latitudes, as expected from a simple population gradient. This exercise proves not only that our technique can be used to determine metallicities of stars precisely from multi-band photometry, but also that we can use corrected synthetic spectra to combine data in various filter sets to generate an internally consistent all-sky metallicity maps. Our calibration procedure is currently valid for main-sequence stars, and has lower precision for giant stars. Consequently, the above mapping in this study based on main-sequence stars probes a local volume out to  $\sim 6$  kpc from the Sun. Giant stars are excluded in our sample using color-magnitude relations based on Gaia parallaxes, but a purely photometric approach can also be employed to tag such stars, as demonstrated in Paper III.

Our photometric technique is a sensitive probe of photometric zero-point errors. It is particularly useful for large photometric surveys because it is non-trivial to have an internally consistent photometric zero point across large areas on the sky. In Appendix B, we demonstrate the existence of spatially correlated photometric zero-point errors in SDSS  $u$  and SMSS  $uv$  based on our corrected models. The size of photometric zero-point offsets is a few hundredth of magnitude level, but is as high as 0.1 mag in some areas. By inverting the problem, zero-point offsets in photometry can be derived to make a uniform mean metallicity of nearby stars on the sky. This backward design on photometric zero-point corrections improves the quality of the metallicity mapping

and somewhat narrows the gap in model deviations between the cluster sequences and the SEGUE sample. For this reason, we iterate the calibration procedure (§ 2) using zero-point corrected photometry in SDSS  $u$  and SMSS  $uv$ . In the following analysis, including Figure 8, all input photometry is corrected for the spatially correlated zero-point offsets. These steps closely parallel similar exercises in zero-point corrections for the SMSS  $uv$  in Huang et al. (2021, 2022).

More quantitative comparisons with previous studies can be made using phase-space diagrams such as shown in Figure 9, in which the number density of stars is displayed as a function of  $v_\phi$  and  $[\text{Fe}/\text{H}]$ . Positive values of  $v_\phi$  indicate that stars are moving in the same direction as the Galactic disk. The displayed data are taken at  $3.5 < |Z| \leq 6$  kpc, where the contribution of disk stars can be minimized (see Paper III). Since Gaia parallaxes have large uncertainties for our main-sequence star sample at this distance, we use metallicity and distance estimates from fully photometric solutions based on SDSS  $\cap$  PS1 photometry, without relying on parallaxes.

The phase-space diagrams in panels (a) and (b) of Figure 9 are taken from  $8 < R_{\text{GC}} \leq 11$  kpc and  $11 < R_{\text{GC}} \leq 14$  kpc, respectively, in Galactocentric spherical coordinates, which reveal complex sub-structures of local stars. The high metallicity, fast-rotating clump at  $\langle v_\phi \rangle \approx 150 \text{ km s}^{-1}$  and  $\langle [\text{Fe}/\text{H}] \rangle \approx -0.5$  in panel (b) represents thick-disk stars. Its mean  $v_\phi$  and  $[\text{Fe}/\text{H}]$  are similar to earlier results in the literature (see Yan et al. 2019, and references therein). On the other hand, metal-rich ( $[\text{Fe}/\text{H}] > -1$ ) stars in panel (a) have a skewed  $v_\phi$  distribution, owing to an increased contribution of the Splash in the inner Galactic region, as demonstrated in Paper III.

In panels (a) and (b) of Figure 9, a group of metal-poor stars is seen at  $[\text{Fe}/\text{H}] \approx -2.2$ , which exhibits a slow net prograde rotation ( $\langle v_\phi \rangle \approx 70 \text{ km s}^{-1}$ ). Along with a more metal-rich ( $[\text{Fe}/\text{H}] \approx -1.5$ ) counterpart in the inner Galactic region, it was seen as one of the main constituents of the Galactic halo in our series of papers. In Paper I, we considered both of these components as “inner and outer halos” in the dual halo paradigm (Carollo et al. 2007, 2010; Beers et al. 2012), but we called them “metal-poor and metal-rich halos” in Paper II. On the other hand, we made a presumption in Paper III that they constitute a main body of GSE, owing to the lack of other analogous structures known in the same phase space.

However, recent evidence suggests that the slowly rotating metal-poor stars are likely a separate entity from GSE. Belokurov & Kravtsov (2022) used aluminium abundances to separate *in situ* stars in the halo from



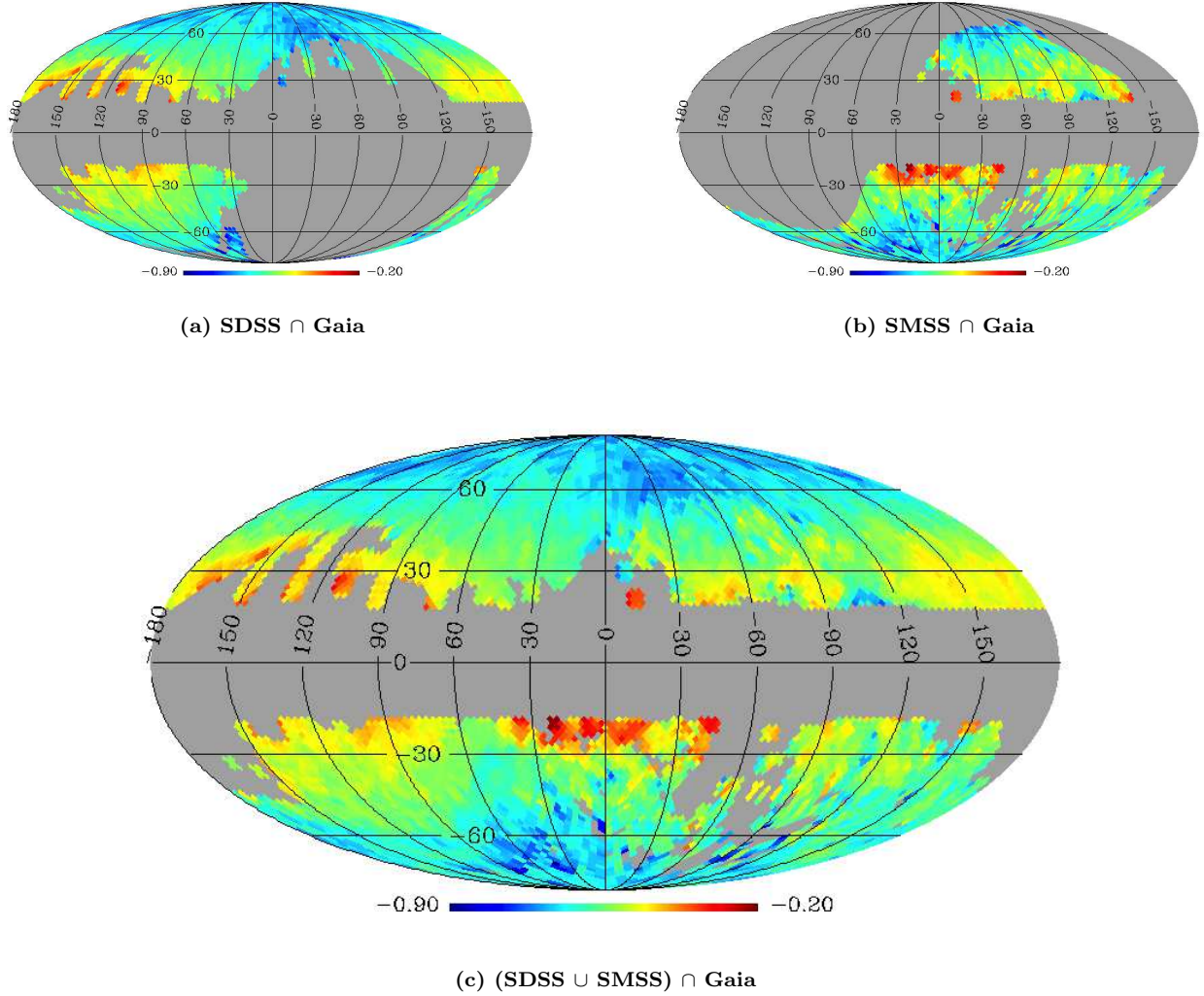


**Figure 8.** A global metallicity map using the Mollweide projection in the Galactic coordinate system. Weighted mean metallicities are shown for stars at  $1.2 < d < 3$  kpc from (a) SDSS, (b) SMSS, and (c) SDSS  $\cup$  SMSS, where PS1 photometry is used if available. All metallicity estimates are derived using Gaia parallaxes. Only stars with  $\sigma_\pi/\pi < 0.3$  and  $|b| > 20^\circ$  are shown, while high-extinction regions with  $E(B - V) > 0.1$  are excluded. Each HEALPix area is  $3.3 \text{ deg}^2$  at  $N_{\text{side}} = 32$ .

accreted stars, and found a large number of metal-poor in situ stars ( $[\text{Fe}/\text{H}] < -1$ ). Although they span an extreme range in  $v_\phi$  (from nearly  $\sim -150 \text{ km s}^{-1}$  to  $\sim 300 \text{ km s}^{-1}$ ) and their spectroscopic sample is limited to  $[\text{Fe}/\text{H}] > -1.5$ , their approximate mean  $v_\phi \sim 100 \text{ km s}^{-1}$  and metallicity ( $[\text{Fe}/\text{H}] < -1$ ) suggest that these stars (dubbed “Aurora”) are a part of the structure seen in our previous work. Given its lower metallicity than the Splash, it is likely an old (primordial) in situ halo that formed before the GSE merger at  $z = 1-2$ .

In support of this view, we employ a simple proper-motion cut in the sample to separate stars in GSE from the metal-poor halo distribution, as demonstrated in panels (c) and (d) of Figure 9. They show the same phase-space diagrams of stars as in panel (b), but have

different ranges of proper motion,  $< 10 \text{ mas yr}^{-1}$  and  $> 10 \text{ mas yr}^{-1}$ , respectively. In panel (c), both the metal-poor in situ halo and thick disk are seen, connected by a narrow band of stars, which we assigned to the Metal-Weak Thick Disk (MWTD) in a Gaussian mixture model in Paper III. On the other hand, an elongated structure along the  $v_\phi = 0 \text{ km s}^{-1}$  line stands out from the high proper-motion sample in panel (d), which encompasses a wide range of metallicity ( $-3 < [\text{Fe}/\text{H}] < -0.5$ ). The chemical and kinematical properties of these high proper-motion stars are similar to GSE in the original works of Belokurov et al. (2018) and Helmi et al. (2018).

Although our  $v_\phi$  measurement is strongly correlated with proper motions, the above separation can be un-

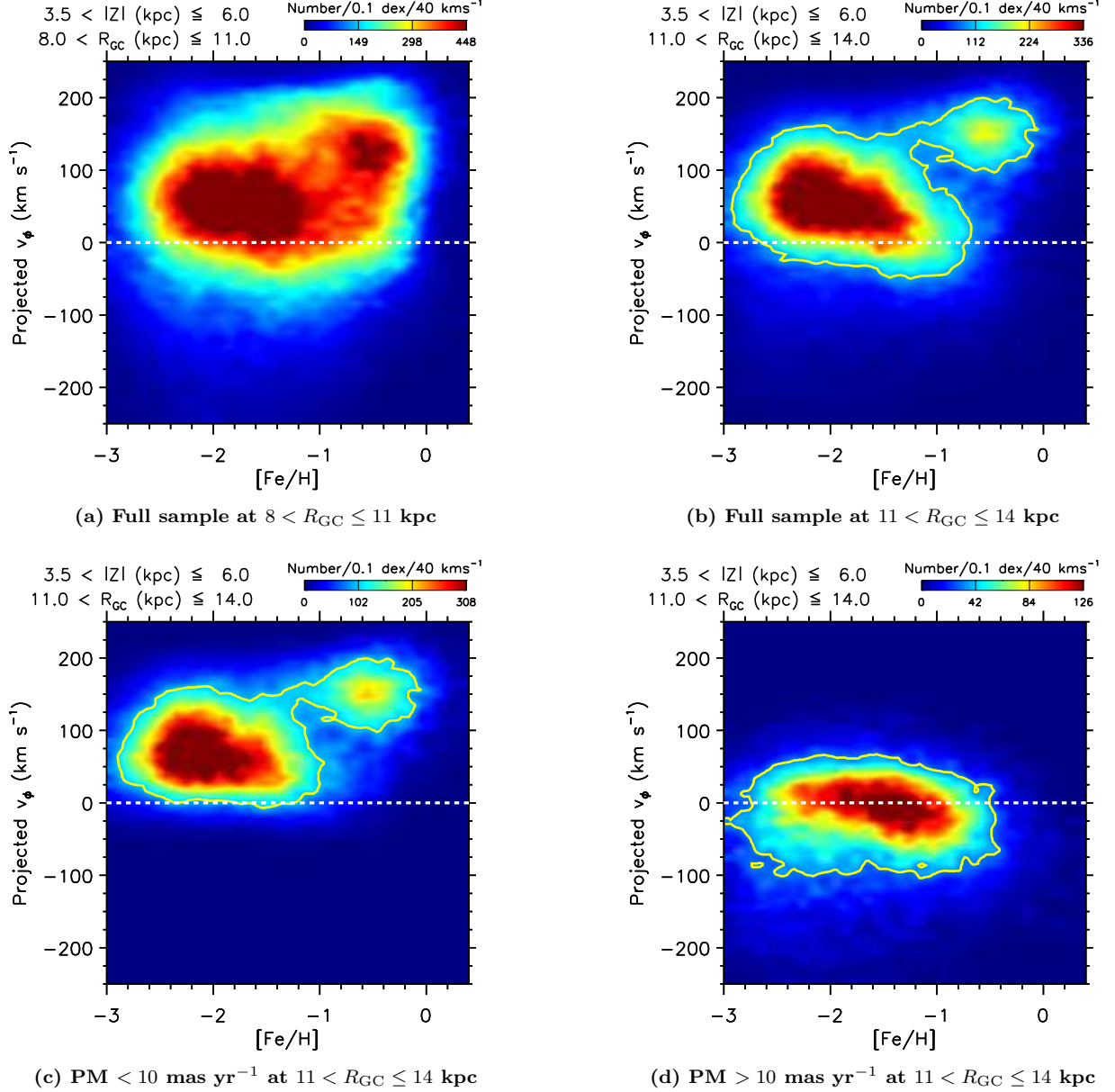


**Figure 9.** Phase-space diagrams based on photometric metallicity and distance estimates from SDSS  $\cap$  PS1 photometry. (a) Stars at  $3.5 < |Z| \leq 6$  kpc and  $8 < R_{\text{GC}} \leq 11$  kpc. (b) A full sample of stars at the same  $|Z|$  as in panel (a), but at  $11 < R_{\text{GC}} \leq 14$  kpc. (c) Same as in panel (b), but from stars having proper motions less than 10 mas yr $^{-1}$ . (d) Same as in panel (b), but for stars having  $> 10$  mas yr $^{-1}$ .

derstood by the highly radial orbits of GSE stars, which contrast with a nearly isotropic velocity distribution of metal-poor in situ halo stars. We also note that the separation does not change appreciably even if the heliocentric distances of the sample are further narrowed down, indicating that smaller (negative)  $v_\phi$  is not merely caused by systematically shorter distances. In summary, all of these chemical and kinematical properties of individual populations in our phase-space diagrams are consistent with those found from previous (mostly spec-

troscopic) studies, which essentially validates our photometric  $[\text{Fe}/\text{H}]$  and  $v_\phi$  estimates.

### 3.2. Scale-Height and Scale-Length Distributions

To study structural properties of each group of stars, we compute a scale length and height in bins of  $v_\phi$  and  $[\text{Fe}/\text{H}]$ , with bin sizes set to 25 km s $^{-1}$  and 0.2 dex, respectively. In each bin, a number density of stars is computed in bins of 500 pc in  $Z$  and  $R$ , respectively,

and is fit using the following exponential function:

$$\rho = \rho_0 e^{-R/L} e^{-Z/H}, \quad (1)$$

where  $L$  and  $H$  represent a scale length and a scale height, respectively, and  $\rho_0$  is a normalization. Although it has been known that bulk halo stars on average follow a power-law density profile, we use equation (1) as a proxy in the local volume near the Galactic plane in order to carry a relative comparison between different populations. Given the cone-shaped survey data volume, a scale height is computed using stars at  $1 < |Z| < 4$  kpc within  $\pm 1$  kpc from the solar radius in each Galactic hemisphere. A scale length is derived from stars across  $7 < R < 12$  kpc, but tailored at  $1 < |Z| < 3$  kpc to include stars at nearly equal  $Z$  over the  $R$  range. Uncertainties in stellar density are computed by taking a standard deviation from the best-fitting model, and the regression is repeated to estimate final uncertainties in the scale measurement.

Figure 10 displays a distribution of scale height in each Galactic hemisphere from the SDSS  $\cap$  Gaia sample. Only those measurements with a fractional distance uncertainty less than 30% are included. A  $0.2 \text{ dex} \times 25 \text{ km s}^{-1}$  pixel is subdivided into  $4 \times 4$  sub-pixels, which are smoothed using a 5-point boxcar average, in order to have a smoothed, global look at changes in the structural properties. Likewise, Figure 11 shows a distribution of scale length in both hemispheres, binned and smoothed in the same manner as in Figure 10. A requirement that stars lie in the stripe along the Galactic prime meridian severely limits the number of stars available in each data set, resulting in  $\approx 4 \times 10^6$  and  $2 \times 10^6$  stars in the Northern and Southern Galactic Hemispheres, respectively.

In the top panels of Figure 10 and 11, three notable features are seen in the Northern Galactic Hemisphere, which are marked by the circled numbers. The intermediate scale-height and scale-length valley is particularly evident, extending from a region mainly occupied by GSE stars (‘①’) to a region populated by the Splash (‘②’). This valley appears even more dramatic, as it contrasts with a scale-height “highland” at  $[\text{Fe}/\text{H}] \approx -1.8$  and  $v_\phi \approx +80 \text{ km s}^{-1}$  (‘③’). For reference, the circled numbers are also marked in the following figures, including the bottom panels of Figures 10 and 11.

The intermediate scale-height valley directly shows that GSE stars are distributed farther from the Galactic plane than disk stars, but not as far as metal-poor in situ halo stars. This observation can be understood by a low inclination, highly radial orbit of the GSE progenitor, which penetrated deep into the primordial Galaxy. In addition, a comparison between the North-

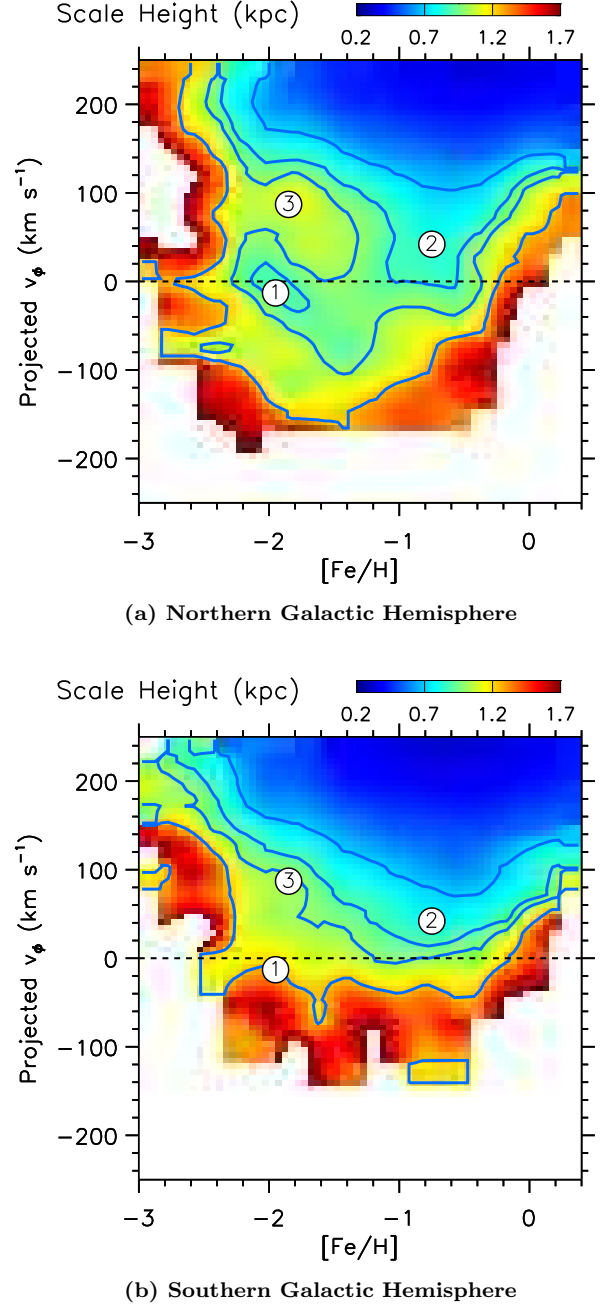
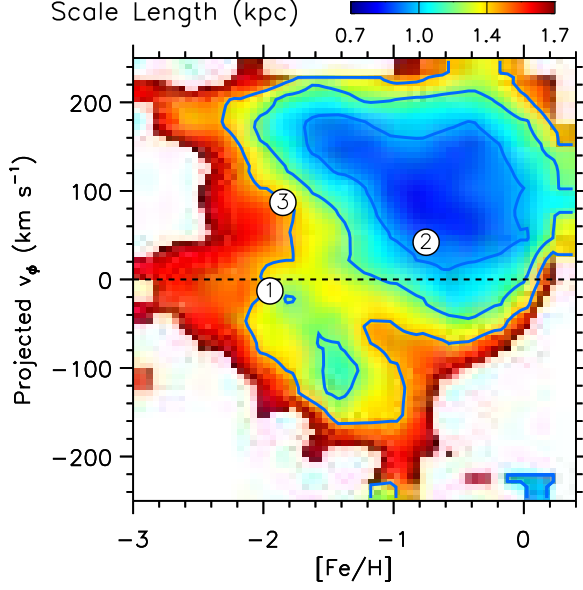
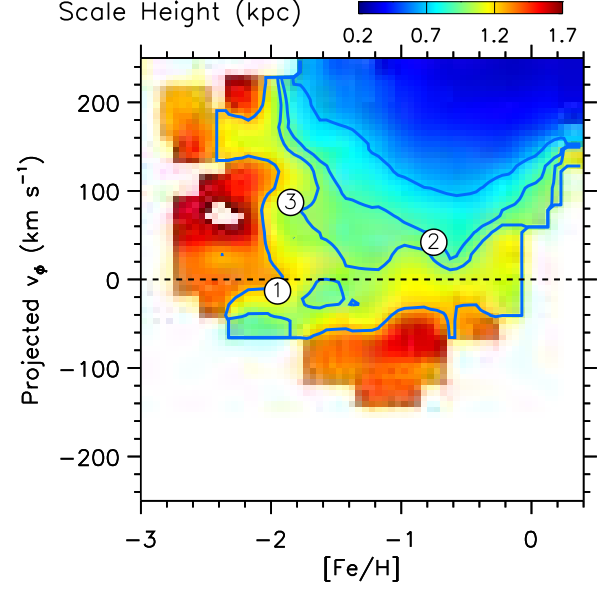


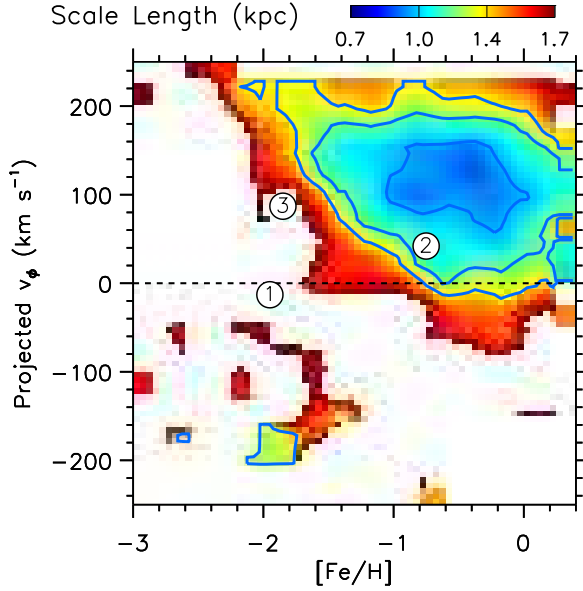
**Figure 10.** Distribution of scale height based on the SDSS  $\cap$  Gaia sample. Results from the Northern and Southern Hemispheres are shown in the top and bottom panels, respectively. Scale heights are computed within a 2 kpc-wide zone centered at the Sun ( $7.34 \leq R \leq 9.34$  kpc). Notable features seen in Panel (a) are marked by circled numbers in both panels: ① GSE, ② Splash, and ③ metal-poor in situ halo.



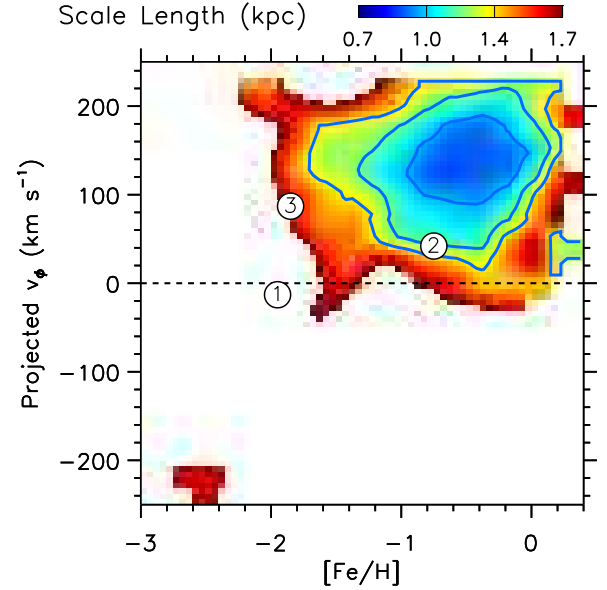
(a) Northern Galactic Hemisphere



(a) Scale height in the Southern Galactic Hemisphere



(b) Southern Galactic Hemisphere



(b) Scale length in the Southern Galactic Hemisphere

**Figure 11.** Distribution of scale length based on the SDSS  $\cap$  Gaia sample in the Northern (top) and Southern Hemisphere (bottom). Scale lengths are computed using stars at  $7 < R < 12$  kpc and  $1 < |Z| < 3$  kpc. The circled numbers are the same as in Figure 10.

ern and Southern Hemispheres in Figures 10 and 11 clearly demonstrates a larger amount of debris in the Northern Hemisphere in the local volume, owing to a pileup of stars at the last apocenter of a highly eccentric orbit of the GSE progenitor (Naidu et al. 2020).

**Figure 12.** Distribution of scale height (top) and scale length (bottom) based on the SMSS  $\cap$  Gaia sample. The circled numbers are the same as in Figure 10.

The asymmetric stellar distribution in the halo between the Northern and Southern Galactic Hemispheres can be checked using SMSS  $\cap$  Gaia. SDSS mainly covers the Northern Galactic Hemisphere, but has a limited coverage in the South. On the other hand, SMSS covers almost the opposite side of the celestial hemisphere



(see Figure 8) with a total of  $\approx 6 \times 10^5$  stars in the Northern Galactic Hemisphere and  $\approx 10^6$  stars in the South in our sample. Figure 12 displays scale-height and scale-length distributions from SMSS  $\cap$  Gaia in the Southern Galactic Hemisphere, generated following the same steps used for Figures 10 and 11. The coherent structure in the parameter space covered by GSE is not seen as clearly as in the Northern Galactic Hemisphere from SDSS  $\cap$  Gaia, but resembles the distributions in the South, highlighting the highly eccentric orbit of the GSE merger. On the other hand, owing to the limited overlap along the Galactic prime meridian, the SDSS  $\cap$  Gaia sample is biased toward the Galactic anticenter direction in the Southern Hemisphere, while the sample from SMSS  $\cap$  Gaia is more populated toward the Galactic center. Therefore, a trace of the intermediate scale-height valley in the top panel could be real, and may capture the GSE debris in the direction toward the Galactic center. Deeper SMSS photometry in future data releases would be useful to explore this volume in more detail.

In the top panel of Figure 10, a vertical trough with intermediate scale heights lies at  $[\text{Fe}/\text{H}] \sim -0.8$ , extending from  $v_\phi \sim 0 \text{ km s}^{-1}$  to  $v_\phi \sim 100 \text{ km s}^{-1}$ . Originally, Belokurov et al. (2020) defined a region occupied by the Splash as  $-0.7 < [\text{Fe}/\text{H}] < -0.2$  and  $-150 < v_\phi < +100 \text{ km s}^{-1}$ , which overlaps with this trough. The fact that the intermediate scale-height valley from GSE stretches out to a region populated by Splash stars supports a previous claim that the GSE merger has dynamically heated stars in the primordial disk of the Milky Way (Bonaca et al. 2017; Belokurov et al. 2020). In other words, because a nearly in-plane collision with a dwarf galaxy would leave behind heated stars confined to a disk plane, this apparent coincidence supports a view on a causal connection between the Splash and GSE. In addition, since such stars originated from the primordial disk of the Galaxy, which was smaller in size than the current stellar disk, this also naturally explains the short scale length of these stars (Figure 11).

If the small scale length is an indication that stars were born in the inner region, and then were displaced by mergers, the vast stretch of the lowland with small scale lengths in Figure 11 implies that dynamical heating took place over a wider range of metallicity than previously considered by Belokurov et al. (2020). At  $[\text{Fe}/\text{H}] > -1$ , stars with the lowest scale length are located at  $v_\phi \sim +100 \text{ km s}^{-1}$ . At lower metallicities, the nearly horizontal trough ( $v_\phi \sim +150 \text{ km s}^{-1}$  at  $[\text{Fe}/\text{H}] \approx -1.5$ ) coincides with the MWTD (see Paper III). If the lowland in the top panel of Figure 11 is fenced by a contour line at  $L = 1.1 \text{ kpc}$  and is taken as an approximate ex-

tent of the dynamical heating from these mean lines, it covers  $-2 < [\text{Fe}/\text{H}] < 0$ . Therefore, even if the GSE progenitor was a major source of the dynamical heating of a primordial disk, it seems unlikely that the orbital properties of stars in this region are altered by a single massive merger event. Instead, our result indicates that such a dynamical heating process on the primordial disk was in operation, even before the GSE merger, driven by more numerous minor mergers, as predicted by numerical simulations of the early universe (e.g., Grand et al. 2020).

The other interesting feature is the “highland” in the scale-height distribution (‘③’ in Figure 10), which coincides with the metal-poor in situ halo (see Figure 9). Its scale height reaches  $H \sim 1.1 \text{ kpc}$ , which is significantly higher than those of heated stars ( $\sim 0.8 \text{ kpc}$ ); therefore, it is unlikely that it formed through the same dynamical heating process. Moreover, the highland exhibits a gradient in the scale length, as shown in the top panel of Figure 11, in the sense that more metal-rich stars are more strongly concentrated in the inner region of the Galaxy. This implies that more active star formation took place in the deeper potential well, while the Milky Way has grown by chaotic coalescence of numerous small gas-rich dwarf galaxies in the early universe. It is unclear, however, how the Milky Way attained the net angular momentum in the same direction as that of the Galactic disk at this stage. Nonetheless, its small prograde net rotation ( $\langle v_\phi \rangle \sim +60 \text{ km s}^{-1}$ ) suggests that it had maintained a puffy disk-like structure owing to turbulent nature of the gas-rich minor mergers.

### 3.3. The Galactic Starburst Sequence (GSS)

Our phase-space diagrams also reveal a long and narrow sequence of stars when a simple cut on proper motion is made. All four panels in Figure 13 are drawn from the same SDSS  $\cap$  Gaia sample, but with different cuts on a minimum value of proper motions (20, 40, 60, and 70  $\text{mas yr}^{-1}$ , respectively). The top left panel is dominated by disk populations (mostly thick-disk stars), but a low  $v_\phi$ , low  $[\text{Fe}/\text{H}]$  tail begins to show up when a mild cut on proper motion (20  $\text{mas yr}^{-1}$ ) is imposed. At  $> 40 \text{ mas yr}^{-1}$ , a striking elbow-like feature emerges from these diagrams, where halo and disk stars form a narrow, continuous sequence over a wide range of  $[\text{Fe}/\text{H}]$  and  $v_\phi$ . This feature is characterized by two joint, orthogonal branches; the horizontal arm is nearly parallel to the  $v_\phi = 0 \text{ km s}^{-1}$  line over a wide range of metallicity ( $-2 \lesssim [\text{Fe}/\text{H}] \lesssim -0.4$ ), while the vertical arm has a narrow metallicity range ( $-0.8 \lesssim [\text{Fe}/\text{H}] \lesssim -0.2$ ). The sequence passes through GSE and the Splash, and is eventually connected to the



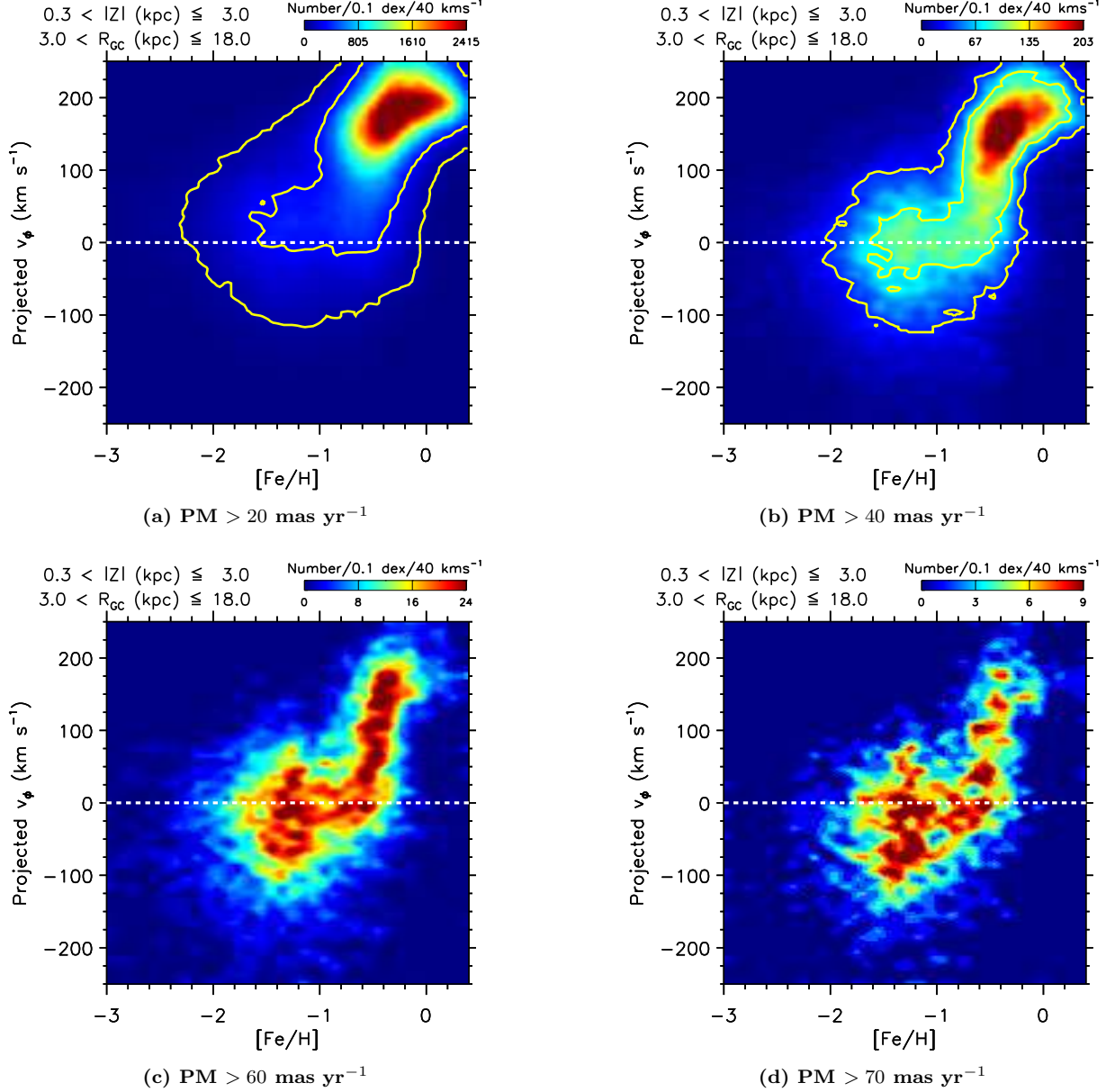


**Figure 13.** A phase-space diagram of stars with large proper motions (PM) from SDSS  $\cap$  Gaia.

disk. Although our  $v_\phi$  estimates depend on distance, the elbow-like feature becomes stronger with higher proper-motion cuts, but changes little with distance from the Sun.

As shown in Figure 14, the sequence persists even when SMSS  $\cap$  Gaia is used, indicating that it is present in both hemispheres. Aside from our photometric metallicities, the same sequence can also be seen in Figure 15, which is based on spectroscopic metallicities in Gaia DR3 from the Radial Velocity Spectrometer (RVS) spectra ( $\lambda/\Delta\lambda = 11,500$ ) using the General Stellar Parameteriser-Spectroscopy (GSP-Spec) module (Recio-Blanco et al. 2022). Because these spectroscopic

observations are available for bright stars ( $G < 14$  mag), the sample is limited to relatively nearby stars ( $1 < |Z| < 2$  kpc); the lower  $|Z|$  cut is made to exclude numerous disk stars. The proper-motion cut is lowered to  $25 \text{ mas yr}^{-1}$  to retain as many stars as possible along the sequence. On the other hand, the constraint on Galactic latitudes is lifted, as the spectroscopic metallicities are only weakly dependent on foreground reddening. While the left panel in Figure 15 is based on the projected  $v_\phi$  as for our photometric samples along the prime meridian, the right panel is based on full three-dimensional space motions from both radial velocities and proper motions in Gaia. The sequence appears almost identical in both

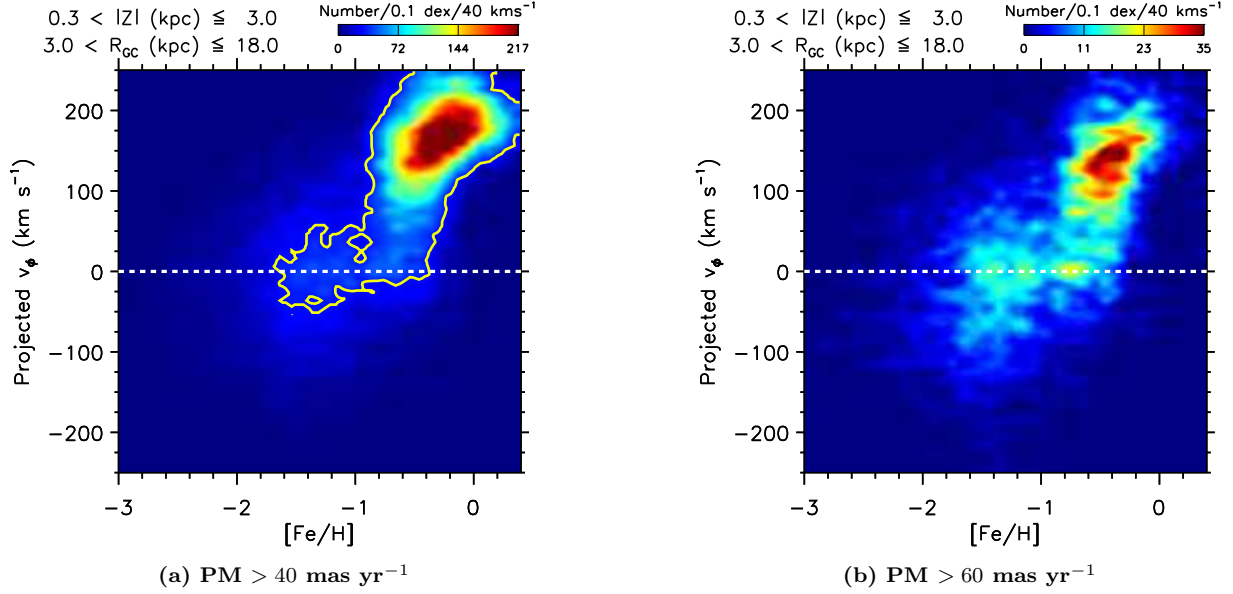


**Figure 14.** Same as in Figure 13, but from SMSS  $\cap$  Gaia.

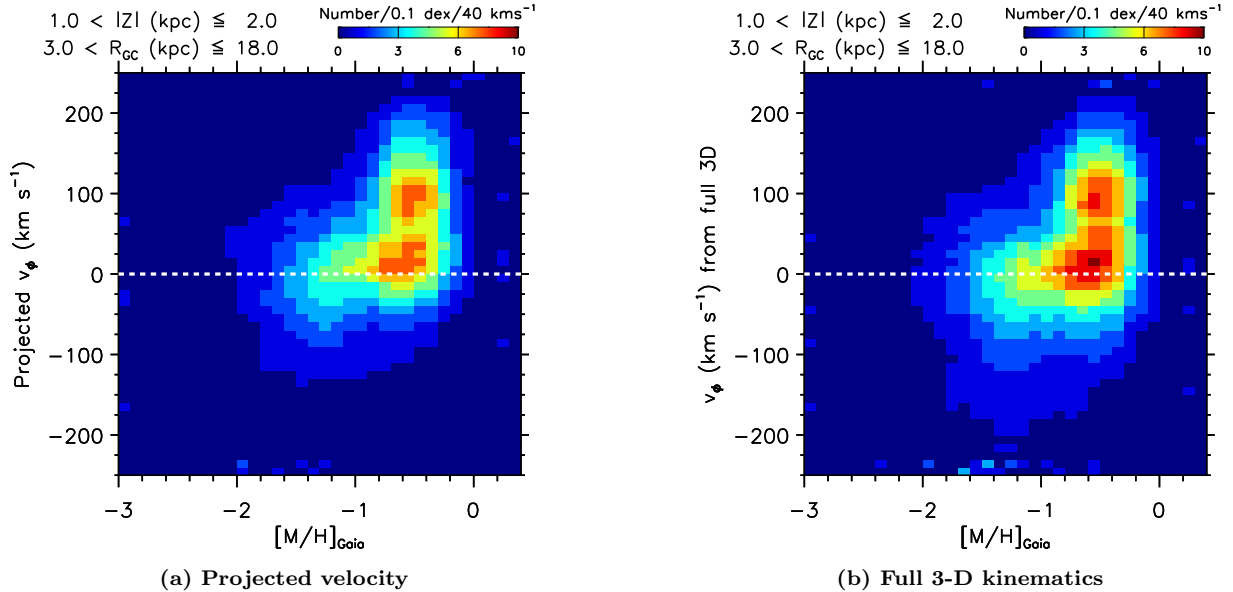


**Figure 15.** (a) Same as in Figure 13, but a phase-space diagram of stars for which Gaia's metallicity estimates are available. A vertical distance range ( $1 < |Z| < 2$  kpc) and a proper-motion cut ( $> 25$  mas yr $^{-1}$ ) are adjusted to emphasize the observed sequence more clearly. (b) Same as in panel (a), but based on three dimensional motions in Gaia.

panels, which supports the existence of this coherent structure. Besides, this also validates our approach for obtaining  $v_\phi$  from proper motions only.

The continuous chain of stars in the phase-space diagram implies that they formed through successive enrichment of metals along this pathway, and somehow it is connected to the GSE merger. Strikingly, the vertical arm of the sequence has a very narrow metallicity range, indicating that these stars formed in a short gas-

depletion time scale without sufficient time for successive enrichment of metals (but with  $\alpha$ -element enhancement from core-collapse supernovae), while star-forming clouds were falling or changing the orientation of an angular momentum vector rapidly from nearly zero to  $\sim 200$  km s $^{-1}$  in  $v_\phi$ . In other words, our result indicates that the young Milky Way went through a phase of starburst activity. For this reason, we refer to this structure as the Galactic Starburst Sequence (GSS). Notably, the

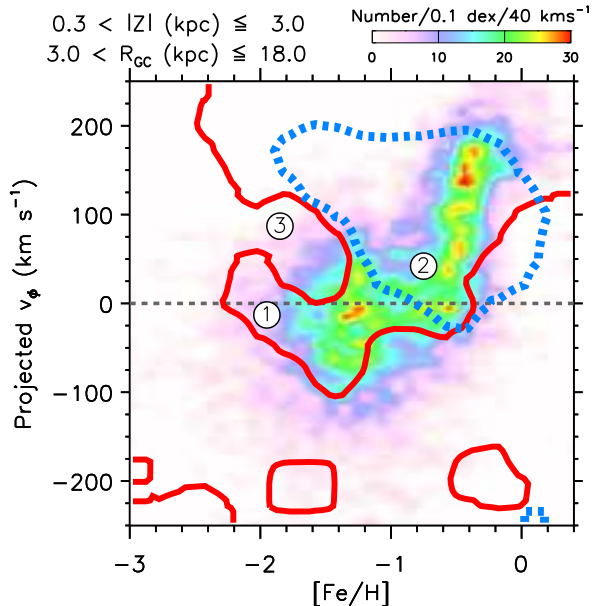


**Figure 16.** Contours of equal scale height (red solid) and length (blue dotted), plotted on top of a phase-space diagram of stars with large proper motions ( $> 60 \text{ mas yr}^{-1}$ ; bottom left panel in Figure 13). The scale-height contour delineates  $H = 1.0 \text{ kpc}$  (top panel of Figure 10), and the scale-length contour has  $L = 1.1 \text{ kpc}$  (top panel of Figure 11).

full GSS is not seen in panel (d) of Figure 9, although it is also made using high proper-motion stars. This difference is manifested by a high central concentration of Splash stars in the Galaxy, as shown in Paper III, and more clearly demonstrated by the short scale lengths in Figure 11. Thus, the GSS is not a dominant structure at large Galactocentric distances.

To better understand the properties of the GSS, we combine the above results in Figure 16. The red solid contour shows a region with a scale height  $H = 1.0 \text{ kpc}$  from the top panel of Figure 10, while the blue dashed contour delineates a scale length  $L = 1.1 \text{ kpc}$  from the top panel of Figure 11. They are overlaid on top of contours of stars with high proper motions ( $> 60 \text{ mas yr}^{-1}$ ) in Figure 13. First, the width of the vertical arm of the GSS is narrower than the metallicity range of the heated population, the extent of which can be delineated by the blue dotted enclosure with a small scale length. This indicates that the Splash, which can be defined as a group of metal-rich stars with halo-like kinematics, is in fact composed of two distinct groups of stars. The first is a group of dynamically heated stars, and the other is the starburst population. Heated stars formed in the inner region of the primordial Galaxy and then were displaced to the current location in the halo, while starburst stars formed in a top-down fashion, as indicated by a weak positive correlation between  $[\text{Fe}/\text{H}]$  and  $v_\phi$ .

Secondly, both GSE and the GSS lie along the intermediate scale-height valley, as shown by the red solid line in Figure 16. The simplest explanation is that the GSE merger has triggered a starburst in the mixture of gas from the primordial Milky Way and gas donated by the GSE merger, because mergers were likely gas rich at high redshifts. According to this scenario, the radially biased orbit of GSE should be responsible for the relatively high transverse motions of stars in the GSS, which contrast with a nearly isotropic velocity distribution of metal-poor in situ halo stars. In other words, these stars formed out of metal-enriched gas having similar orbital properties with the GSE progenitor. Therefore, they are expected to show up in the high proper-motion sample, even though their orbits have evolved significantly over time from halo-like to disk-like orbits.

#### 4. SUMMARY AND DISCUSSIONS

Thanks to Gaia and large-scale photometric and spectroscopic databases, it is now possible to perform accurate comparisons of theoretical models to extensive, high-quality data. In this work, we use models generated using YREC and MARCS, and quantify model deviations as a function of  $T_{\text{eff}}$ , metallicity, and wavelength. The current approach relies on a comparison with multi-wavelength ultra-violet, optical, and near-infrared color- $T_{\text{eff}}$  relations derived from Galactic cluster sequences, Gaia’s double sequence, and a sample of spectroscopic data in SEGUE and GALAH, using photometric data in a number of broad-band filters from SDSS, SMSS, and APASS and standard-star photometry in the literature. Mean flux deviations are derived as a function of wavelength, which amount to up to  $\sim 20\%$  at  $< 4000 \text{ \AA}$ , but significantly less in longer wavelengths. We find that no single factor can remove the observed offsets, but it is more likely a problem arising from a combination of various sources of errors in the models and/or observational data. Subsequently, we define the model offset as an empirical correction function for our specific choice of models.

When combined with proper-motion measurements from Gaia, our technique can be used to construct phase-space ( $v_\phi$  versus  $[\text{Fe}/\text{H}]$ ) diagrams of stars to provide a global perspective on the stellar populations in the Milky Way. In this way, we identify a long and narrow sequence of stars in a phase-space diagram, which we call the GSS. The GSS overlaps with GSE, and runs along a valley with intermediate scale heights, suggesting that GSE has likely triggered star formation. It also passes through the Splash, showing rapid evolution of  $v_\phi$  of star-forming clouds within a narrow metallicity range, which testifies to a starburst event in the young

Milky Way. The wide metallicity range of dynamically heated stars as traced by small scale-length regions in a phase-space diagram indicates that the Splash is likely composed of two stellar populations with distinct origins – dynamically heated and starburst populations.

The double sequence of stars with high transverse motions ( $> 200 \text{ km s}^{-1}$ ) in Gaia (Gaia Collaboration et al. 2018a) is another manifestation of the GSS. As shown in Paper II, the two sequences are separated by a few tenths of a magnitude in *griz* colors, and more strongly when the *u*-band is included, indicating a metallicity offset by  $\sim 1$  dex. According to the corresponding metallicity ranges, stars on the blue sequence belong to GSE, while stars in the red sequence mostly constitute the Splash or, more specifically, the vertical arm of the GSS. Our new perspective into the phase-space diagram of these stars reveals two consecutive modes of chemo-kinematical evolution: a rapid chemical enrichment along the orbit of GSE, followed by starburst in rapidly evolving orbits of gas clouds.

Previously, Necib et al. (2020) identified a group of  $\sim 100$  stars in the solar vicinity, dubbed “Nyx”, which show coherent radial ( $134 \text{ km s}^{-1}$ ) and azimuthal ( $130 \text{ km s}^{-1}$ ) motions. Their metallicities peak at  $[\text{Fe}/\text{H}] = -0.55$ , with a dispersion of 0.13 dex. In addition, they are mostly confined to a plane with a maximum vertical distance of  $Z = 1.7 \text{ kpc}$ , which is comparable to our scale-height measurement ( $H \approx 0.7 \text{ kpc}$ ) for stars having similar  $[\text{Fe}/\text{H}]$  and  $v_\phi$  as Nyx stars (Figure 10). The mean metallicity and a small scale height suggest its close connection to stars in the vertical arm of the GSS. Nonetheless, most of Nyx stars have  $100 \lesssim v_\phi < 250 \text{ km s}^{-1}$ , with a few extreme cases, and therefore trace only the upper half of the vertical arm. Necib et al. (2020) postulated that the Nyx stream is a remnant of a disrupted dwarf galaxy. However, a more recent analysis in Zucker et al. (2021) argues against their extragalactic origin, based on the fact that a subset of these stars are indistinguishable from thick-disk stars in the elemental-abundance space, having larger  $\alpha$ -element abundances than those of accreted stars at a given metallicity.

In other studies, age-metallicity relations also reveal a chain of metal-rich stars, establishing a link between the halo and the disk (Haywood et al. 2013; Nissen et al. 2020; Xiang & Rix 2022). Recently, Xiang & Rix (2022) used  $\alpha$ -element-rich stars with low orbital angular momenta, and demonstrated the existence of a narrow and continuous age-metallicity relation in the Milky Way. According to their analysis, the Milky Way achieved a high metallicity floor ( $[\text{Fe}/\text{H}] \sim -1$ ) about 13 Gyr ago, with successive metal enrichment over the follow-

ing  $\sim 5$  Gyr. The majority of stars are found in a narrow metallicity range ( $-0.7 < [\text{Fe}/\text{H}] < -0.2$ ), which leads to its possible connection to the vertical arm of the GSS. Importantly, its narrow and continuous channel of stars reinforces the physical entity of the GSS.

In addition, recent numerical simulations in the literature also predict the existence of starburst populations in the Milky Way-size galaxies (Cooper et al. 2015; Bignone et al. 2019; Grand et al. 2020; Renaud et al. 2021). For instance, in Grand et al. (2020), a merger with a gas-rich GSE-like progenitor induces starburst activity owing to the increased compression of gas clouds in both galaxies. The star-formation rate suddenly increases by a factor of two, which lasts less than 1 Gyr. Interestingly, these simulations reproduce some of the key features observed in our data, in that both starburst and heated populations produced by the merger event are present in a narrow metallicity bin, but cover a wide range of  $v_\phi$ . Furthermore, the heated population shows a correlation between  $[\text{Fe}/\text{H}]$  and  $v_\phi$  in their simulation, while there is essentially no such dependence for the starburst population (considering an excessively large scatter in  $v_\phi$  at a given metallicity). This may well be explained by a narrow range in  $[\text{Fe}/\text{H}]$  of the vertical arm of the GSS. Another intriguing aspect is that the starburst population in the simulation exhibits a centrally concentrated, rotationally supported disk. This prediction is also in agreement with the fact that the high proper-motion stars are found along the intermediate scale-height valley.

The vertical and horizontal arms of the GSS can be attributed to stars formed during a merger-induced star formation and those accreted from the GSE progenitor, respectively. In our phase-space diagram in Figures 13 and 14, we count each group of stars using a simple box criterion:  $-50 < v_\phi \leq 200 \text{ km s}^{-1}$  and  $-0.9 < [\text{Fe}/\text{H}] \leq 0$  for the starburst, and  $-60 < v_\phi \leq +60 \text{ km s}^{-1}$  and  $-2 < [\text{Fe}/\text{H}] \leq -0.9$  for the accreted population, respectively. We find that the ratios between these two populations are 1.2–4.4, depending on the proper motion cut made in each subset. These estimates qualitatively agree with Grand et al. (2020), in that the total mass of stars formed during a merger-induced star formation in the host galaxy exceeds the stellar mass of accreted stars. Strikingly, they are quantitatively in agreement with a ratio of  $\sim 2$ –5 predicted by a more recent numerical simulation in Orkney et al. (2022).

At high  $v_\phi$ , the GSS is connected to the disk, suggesting that disk stars formed in part from gas clouds left behind after the starburst episode. Interestingly, the mean metallicity of the tip of the GSS ( $[\text{Fe}/\text{H}] \approx -0.4$ ) is coincident with the low-metallicity end of the thin



disk, if the disk stars are divided into the low and high  $\alpha$ -element sequences on the  $[\alpha/\text{Fe}]-[\text{Fe}/\text{H}]$  plane (e.g., [Hayden et al. 2015](#), and references therein). This implies that old stars in the low- $\alpha$  sequence were formed out of a mixture of gas clouds in the protogalactic disk and those accreted by the GSE merger, possibly through the classical “two-infall” model ([Chiappini et al. 1997](#); [Brook et al. 2007](#); [Buck 2020](#)). The lower metallicity of old thin-disk stars than those of the most metal-rich thick-disk stars and their intermediate  $[\alpha/\text{Fe}]$  can be understood by the dilution of the metal-rich clouds in the protogalactic disk and a boost in  $[\alpha/\text{Fe}]$  by core-collapse supernovae during the starburst.

Our finding naturally explains the G-dwarf problem as well — the apparent excess of metal-rich stars in the local disk compared to the prediction from a simple closed-box chemical model (e.g., [Greener et al. 2021](#)). The above interpretation is further supported by recent findings on in situ stars that lie between the GSE and the low- $\alpha$  sequence ([Myeong et al. 2022](#)) and the fraction of Splash stars that exhibit intermediate  $[\alpha/\text{Fe}]$  (Lee, A. et al. 2022, submitted).

The extensibility of calibrated synthetic spectra presented in this work enables accurate predictions of stellar magnitudes for filter passbands in various photometric surveys, such as the Javalambre/Southern Photometric Local Universe Survey (J/S-PLUS; [Cenarro et al. 2019](#); [Mendes de Oliveira et al. 2019](#)) and the Legacy Survey of Space and Time (LSST; [Ivezic et al. 2019](#)). Our metallicity-mapping technique can serve as a useful resource for studying the demographics of stellar populations that are yet to be discovered in the local universe.

## ACKNOWLEDGMENTS

We thank Donald M. Terndrup and Christopher A. Onken for carefully checking our manuscript and providing a number of helpful comments. D.A. thanks Anirudh Chiti for a useful discussion. T.C.B. and Y.S.L. thank Andreia Carrillo for an enlightening discussion on the Galactic starburst. D.A. acknowledges support provided by the National Research Foundation (NRF) of Korea grant funded by the Ministry of Science and ICT (No. 2021R1A2C1004117). T.C.B. and Y.S.L. acknowledge partial support for this work from grant PHY 14-30152; Physics Frontier Center/JINA Center for the Evolution of the Elements (JINA-CEE), and OISE-1927130: The International Research Network for Nuclear Astrophysics (IRENA), awarded by the US National Science Foundation. Y.S.L. acknowledges support from the NRF of Korea grant funded by the Ministry of Science and ICT (NRF-2021R1A2C1008679). T.M. acknowledges financial support from the Spanish Ministry of Science and Innovation (MICINN) through the Spanish State Research Agency, under the Severo Ochoa Program 2020-2023 (CEX2019-000920-S) as well as support from the ACIISI, Consejería de Economía, Conocimiento y Empleo del Gobierno de Canarias and the European Regional Development Fund (ERDF) under grant with reference PROID2021010128.

Funding for the Sloan Digital Sky Survey IV has been provided by the Alfred P. Sloan Foundation, the U.S. Department of Energy Office of Science, and the Participating Institutions. SDSS-IV acknowledges support and resources from the Center for High Performance Computing at the University of Utah. The SDSS website is [www.sdss.org](http://www.sdss.org).

SDSS-IV is managed by the Astrophysical Research Consortium for the Participating Institutions of the SDSS Collaboration including the Brazilian Participation Group, the Carnegie Institution for Science, Carnegie Mellon University, Center for Astrophysics — Harvard & Smithsonian, the Chilean Participation Group, the French Participation Group, Instituto de Astrofísica de Canarias, The Johns Hopkins University, Kavli Institute for the Physics and Mathematics of the Universe (IPMU) / University of Tokyo, the Korean Participation Group, Lawrence Berkeley National Laboratory, Leibniz Institut für Astrophysik Potsdam (AIP), Max-Planck-Institut für Astronomie (MPIA Heidelberg), Max-Planck-Institut für Astrophysik (MPA Garching), Max-Planck-Institut für Extraterrestrische Physik (MPE), National Astronomical Observatories of China, New Mexico State University, New York University, University of Notre Dame, Observatório Na-



cional / MCTI, The Ohio State University, Pennsylvania State University, Shanghai Astronomical Observatory, United Kingdom Participation Group, Universidad Nacional Autónoma de México, University of Arizona, University of Colorado Boulder, University of Oxford, University of Portsmouth, University of Utah, University of Virginia, University of Washington, University of Wisconsin, Vanderbilt University, and Yale University.

This work presents results from the European Space Agency (ESA) space mission Gaia. Gaia data are being processed by the Gaia Data Processing and Analysis Consortium (DPAC). Funding for the DPAC

is provided by national institutions, in particular the institutions participating in the Gaia MultiLateral Agreement (MLA). The Gaia mission website is <https://www.cosmos.esa.int/gaia>. The Gaia archive website is <https://archives.esac.esa.int/gaia>.

This paper makes use of data from the AAVSO Photometric All Sky Survey, whose funding has been provided by the Robert Martin Ayers Sciences Fund and from the NSF (AST-1412587).

*Facilities:* AAVSO, PS1, SkyMapper, Sloan

*Software:* GNU parallel (Tange 2021)

## APPENDIX

### A. CONSTRUCTION OF THE GAIA DOUBLE SEQUENCE AND MODEL COMPARISONS

Here, a number of complementary plots are provided for some selected data sets, which are used in our model calibration (§ 2). Figure 17 displays Gaia’s double sequences in SDSS, SMSS, PS1, and APASS using color indices containing  $u$  or  $B$  passbands, which best separate the blue and red sequences of stars having  $-150 < v_\phi \leq 150$  km s $^{-1}$ . Figure 18 displays comparisons of the original models (without empirical corrections) with Stetson’s cluster photometry. Model comparisons with the SEGUE sample ( $-0.5 < [\text{Fe}/\text{H}] < -0.3$ ) are shown in Figures 19–22 in SDSS, SMSS, PS1, and APASS photometry, respectively. See Paper II for more information on the construction of Gaia’s double sequence and model comparisons of the cluster and the Gaia double sequence in the SDSS filter set.

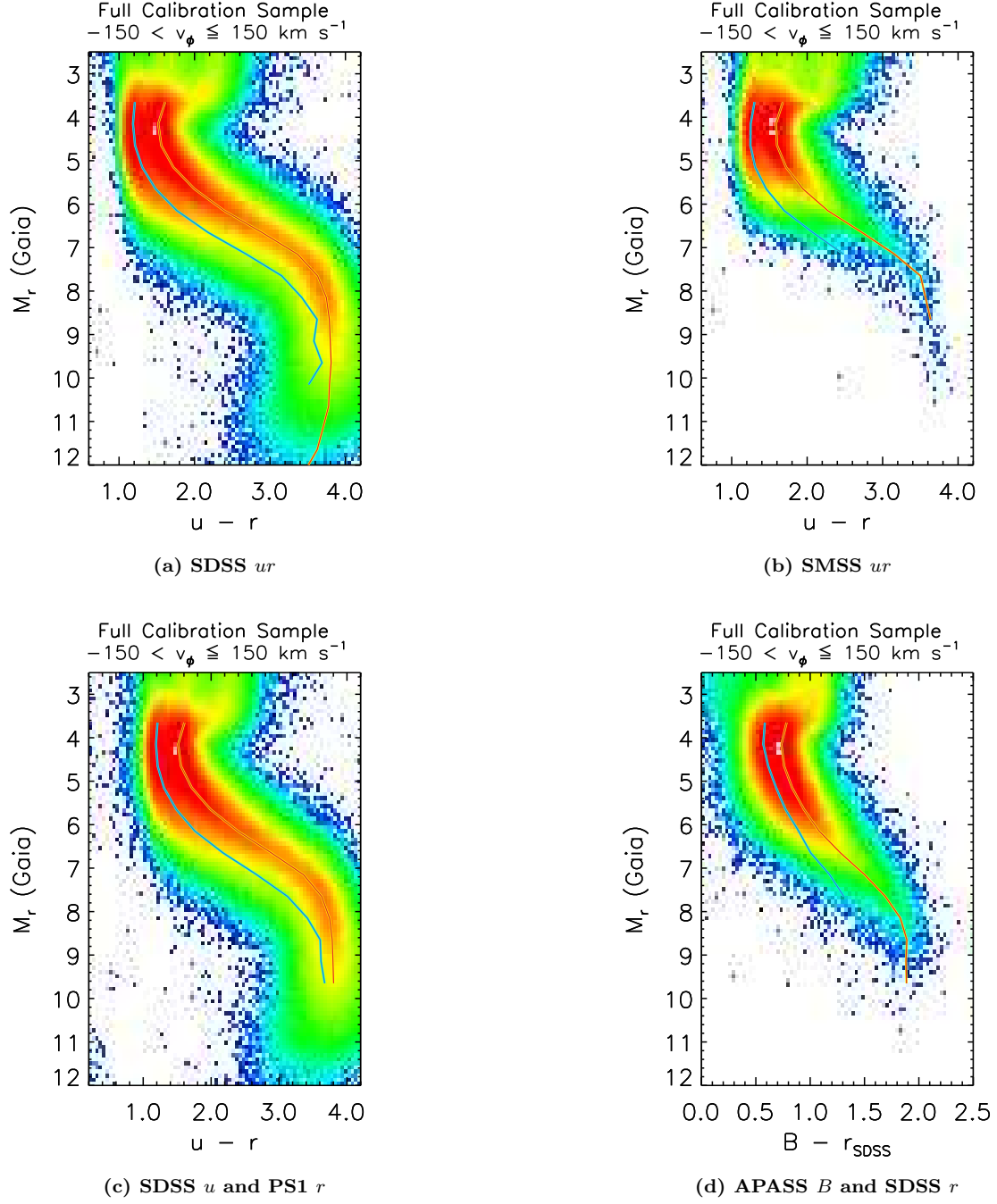


**Figure 17.** Gaia's double sequence in selected passbands. The colored histogram shows a number density of stars with  $-150 < v_\phi \leq +150 \text{ km s}^{-1}$ . The blue and red lines are our derived fiducial sequences.

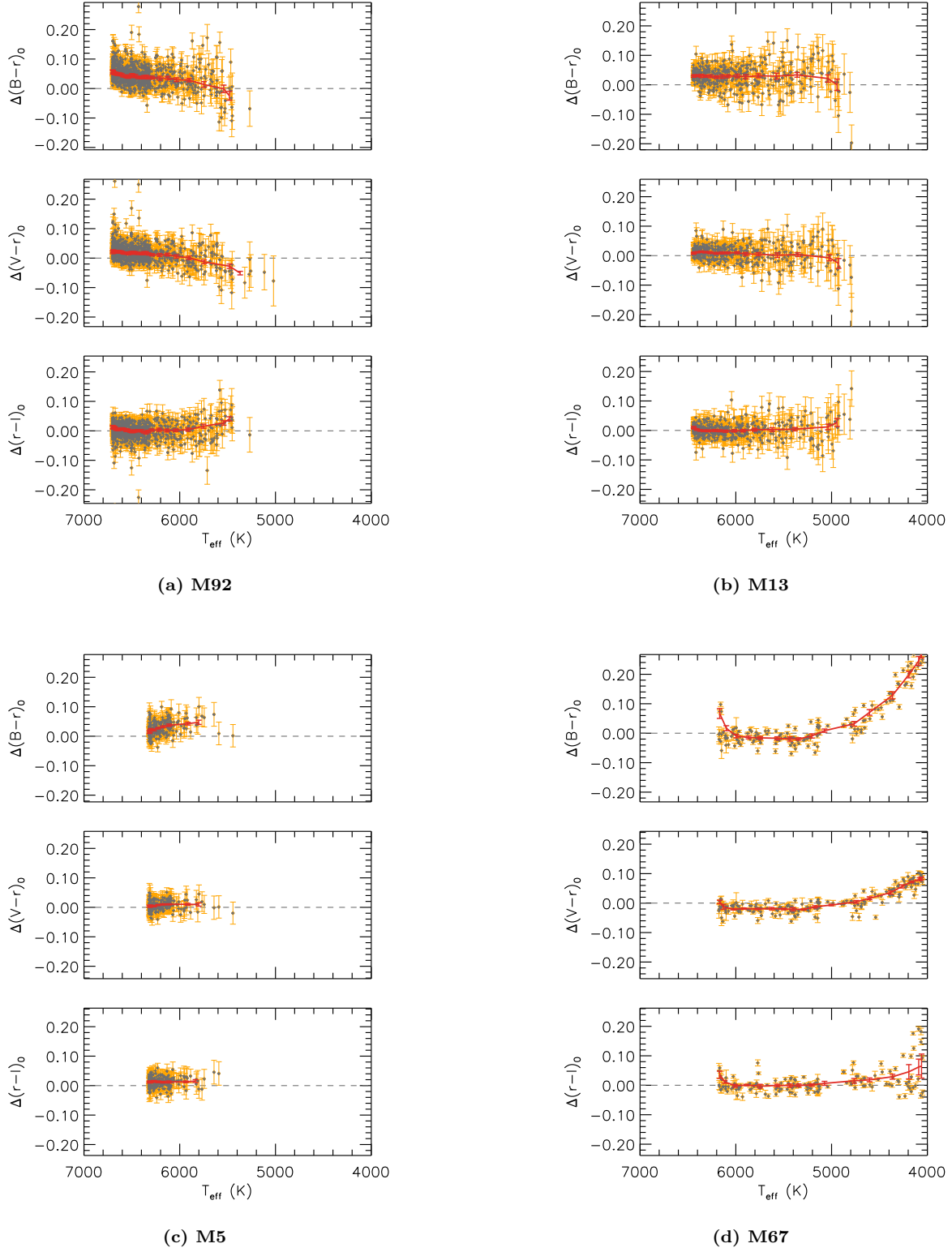


**Figure 18.** Comparisons of Stetson's photometry with theoretical models for selected clusters.

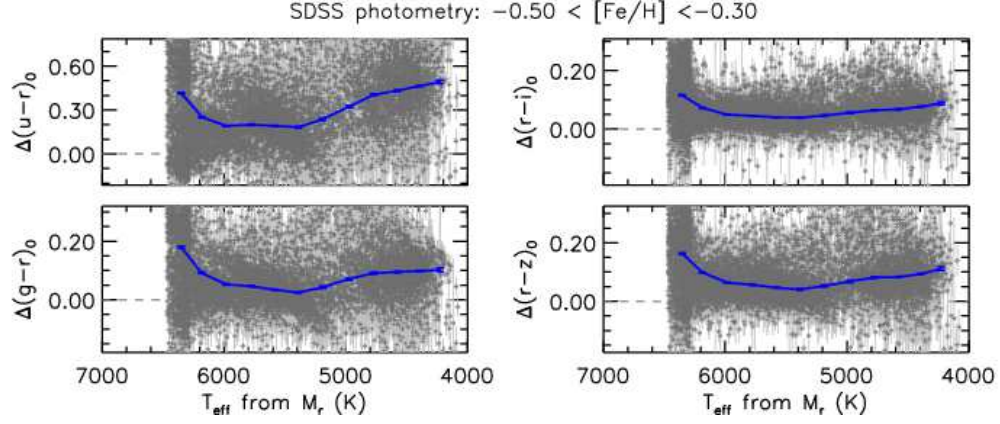


**Figure 19.** Comparison between the observed and original model colors for the SEGUE sample in the SDSS passbands. The above example shows differences of extinction-corrected colors using stars at  $-0.5 < [\text{Fe}/\text{H}] < -0.3$  as a function of photometric  $T_{\text{eff}}$ . The solid line shows average differences in moving boxes, and the error bars indicate uncertainties of the mean values.

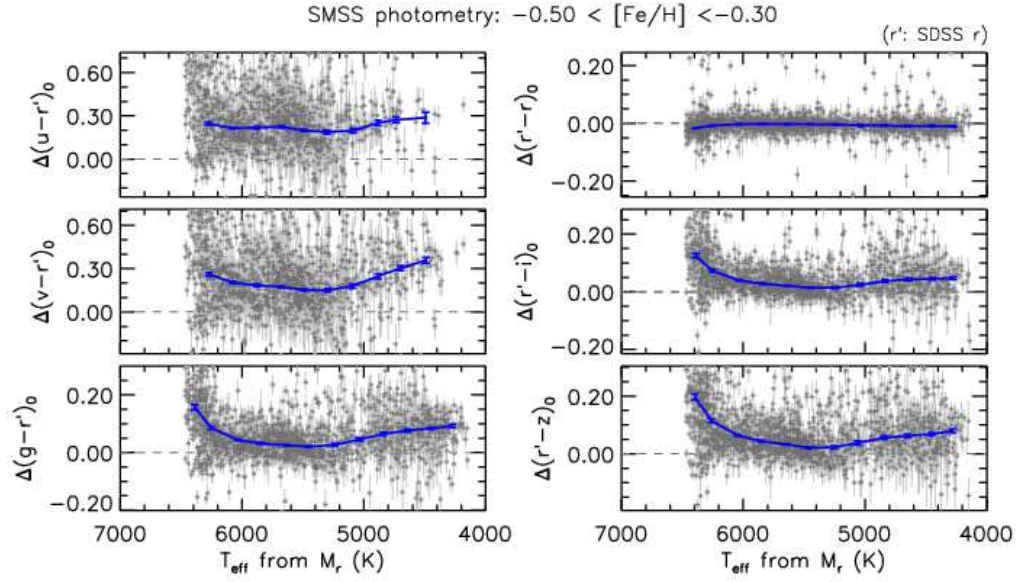


**Figure 20.** Same as in Figure 19, but in the SMSS filters. To avoid confusion, SDSS  $r$  is shown as  $r'$ .

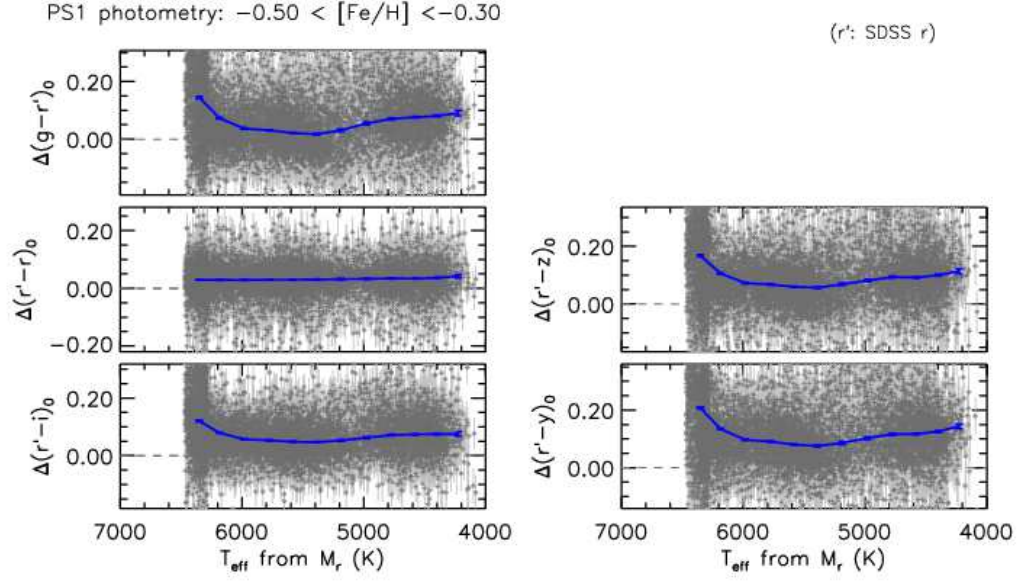


**Figure 21.** Same as in Figure 19, but in the PS1 filters. To avoid confusion, SDSS  $r$  is shown as  $r'$ .

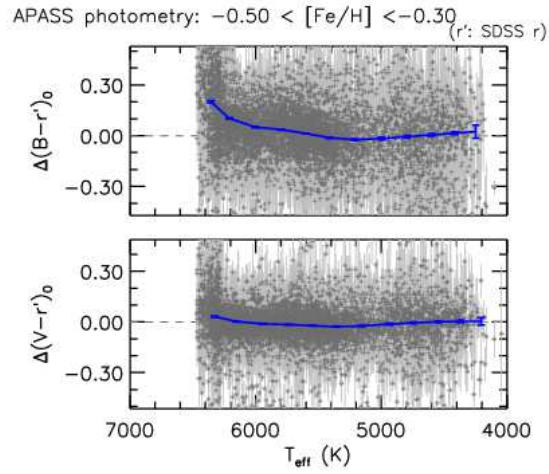


**Figure 22.** Same as in Figure 19, but in the APASS filters. To avoid confusion, SDSS  $r$  is shown as  $r'$ .



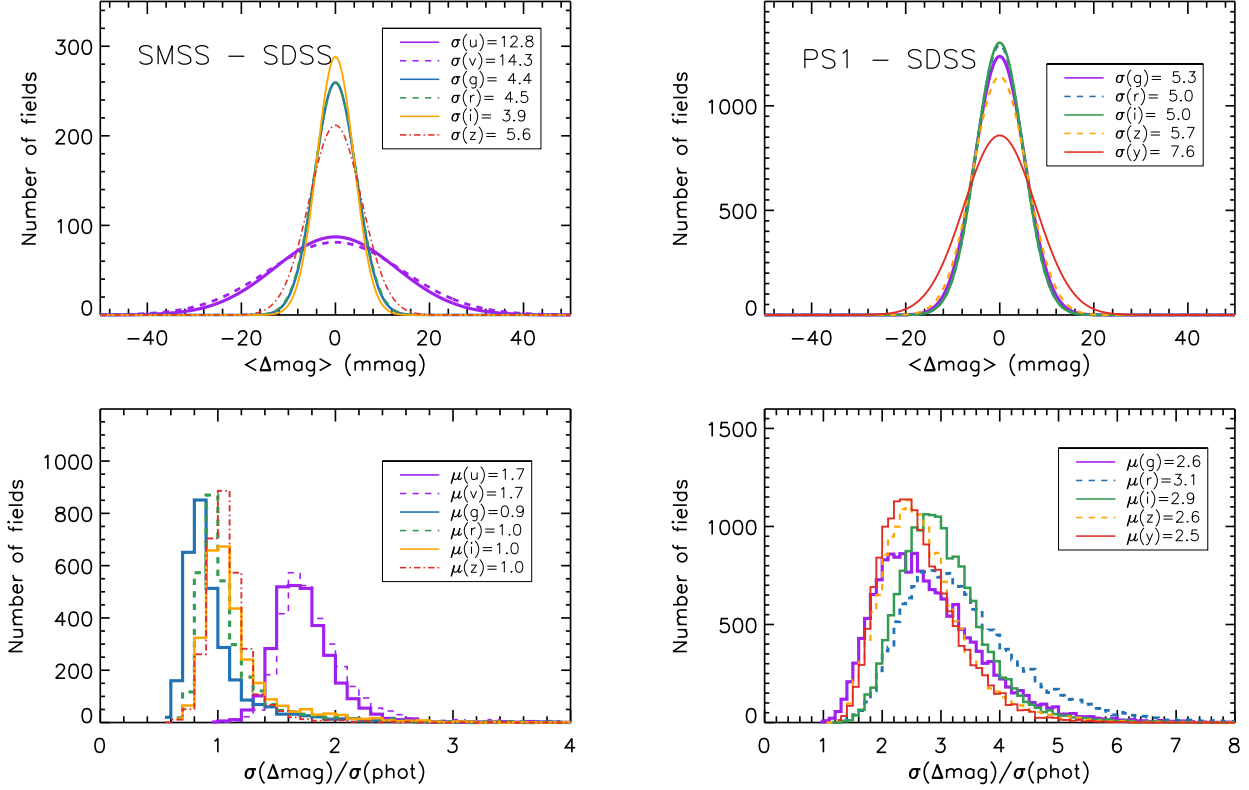


**Figure 23.** Statistical properties of SMSS (left) and PS1 photometry (right) from comparisons with SDSS. Top: A best-fitting Gaussian distribution of magnitude offsets in each passband, after subtracting a color-dependent difference between different passbands. Standard deviations are shown in the inset. Bottom: A distribution of the ratio between a standard deviation of a magnitude difference  $[\sigma(\Delta \text{mag})]$  and a propagated uncertainty  $[\sigma(\text{phot})]$  in each filter passband. The mean ratios are shown in the inset. Both SMSS  $u$ - and  $v$  bands are compared to SDSS  $u$ , and PS1  $y$  to SDSS  $z$ .

## B. PHOTOMETRIC PROPERTIES OF SDSS, SMSS, AND PS1

### B.1. Random and Zero-Point Uncertainties

Since observations in various filter passbands are combined to derive a set of parameters in this study, it is necessary to adopt realistically sized photometric uncertainties in the  $\chi^2$  statistics. Here, we compare SMSS and PS1 photometry with SDSS, and compute a mean magnitude difference and a dispersion to infer the size of the true uncertainties. The comparison with SMSS is limited to narrow regions, since the imaging stripes of SDSS overlaps only a little with SMSS footprints along the celestial equator. The overlap with PS1 is more extensive, as both surveys covered the Northern Hemisphere.

Figure 23 shows statistical properties of the comparison of SDSS photometry with SMSS (left) and PS1 (right), respectively. The top panels display a distribution of a magnitude difference of bright ( $14.5 < r < 18$  mag) stars in each passband. To take into account non-negligible color terms between different filter passbands (i.e., color transformations), the magnitude differences in each  $1^\circ$ -wide strip in R.A. are fit using a third-order polynomial as a function of  $g - r$  in  $0.3 < g - r < 1.1$ , and its mean trend is removed. The SMSS  $v$  is compared to SDSS  $u$ , and PS1  $y$  to SDSS  $z$ .

A weighted median difference is computed in each  $(\Delta\alpha, \Delta\delta) = (1^\circ, 1^\circ)$  region, and an ensemble of these differences are fit using a Gaussian function, as shown by solid lines in the top panels of Figure 23. Standard deviations of the best-fitting Gaussian functions provide a measure of the spatial variation of the photometric zero points across the sky. They are  $\sigma_{\text{zp}}^{\text{SMSS}}(u, v, g, r, i, z) = \{13, 14, 4, 4, 4, 6\}$  mmag and  $\sigma_{\text{zp}}^{\text{PS1}}(g, r, i, z, y) = \{5, 5, 5, 6, 8\}$  mmag, respectively, which are comparable to the quoted systematic uncertainties by each survey.

The bottom panels of Figure 23 show ratios between the standard deviation of a magnitude difference and a propagated uncertainty for each filter passband in each  $(\Delta\alpha, \Delta\delta) = (1^\circ, 1^\circ)$  patch. Again, SMSS  $v$  is compared to SDSS

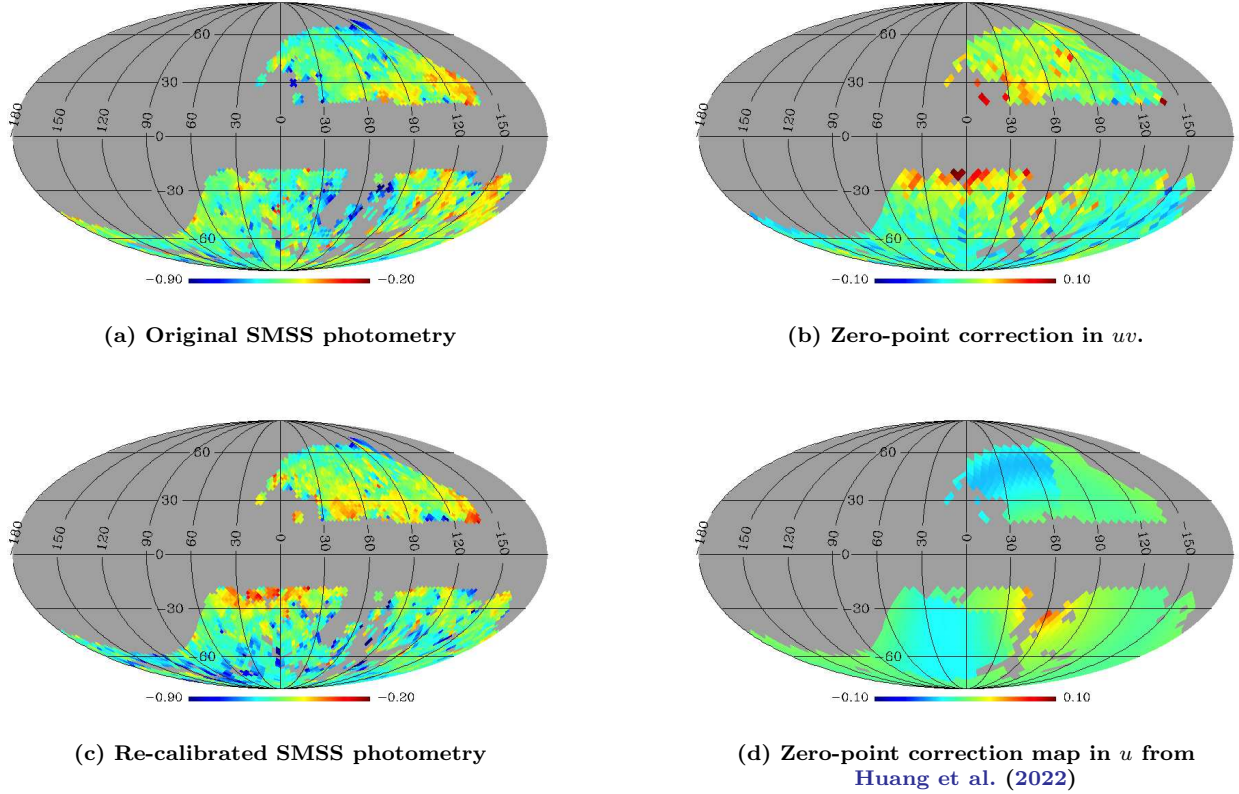


**Figure 24.** Panel (a): A projection map of mean metallicities in the Galactic coordinate system based on the original photometry. The color scheme shows a mean metallicity of stars at  $1.2 < d < 3$  kpc from a generalized histogram in each pixel. Panel (b): Zero-point corrections on  $u$ -band and  $v$ -band photometry, in order to match the peak metallicities of nearby stars ( $0.5 < d < 1$  kpc) to a reference value (see text). Panel (c): Same as in panel (a), but based on the re-calibrated  $uv$  photometry. Panel (d): Zero-point corrections in the  $u$ -band in Huang et al. (2022). In all panels, the Galactic center is at the center, and the North Galactic Pole is to the top. Areas at low Galactic latitudes ( $|b| < 20^\circ$ ) and large cumulative extinction [ $E(B - V) > 0.1$ ] are excluded. Note that the above metallicity maps are not exactly the same as in Figure 8, owing to different ways of estimating metallicities with and without Gaia parallaxes, respectively.

$u$ , and PS1  $y$  to SDSS  $z$ . Some of the brightest objects are rejected in this comparison, owing to unrealistically small uncertainties in the SDSS PSF  $i$  magnitude ( $< 0.005$  mag). As shown in the bottom left panel, the ratios for the SMSS and SDSS  $grz$  are near unity, indicating that photometric uncertainties are comparable to the observed scatter, while photometric uncertainties in  $uv$  are likely under-estimated. As shown in the bottom right panel, the differences between propagated uncertainties and observed dispersions are even larger for PS1 passbands.

Based on the above comparisons, an uncertainty ‘floor’ ( $\sigma_f$ ) is computed in each passband in order to make a median of a standard deviation equal to a median of propagated uncertainties from all  $1^\circ \times 1^\circ$  patches. Assuming that quoted uncertainties in SDSS are correct, we find  $\sigma_f^{\text{SMSS}}(u, v, g, r, i, z) = \{42, 42, 10, 9, 9, 10\}$  mmag and  $\sigma_f^{\text{PS1}}(g, r, i, z, y) = \{43, 44, 42, 44, 43\}$  mmag for SMSS and PS1, respectively. In all cases, zero-point uncertainties ( $\sigma_{zp}$ ) are overwhelmed by the uncertainty floors ( $\sigma_f$ ). We add both uncertainties in quadrature to the original photometric uncertainties in SMSS and PS1, and use them throughout this work.

### B.2. Re-calibration of SMSS $uv$ -Band Photometry

By design, the zero point of SMSS DR2 photometry was set based on  $griz$  photometry in the PS1 system calculated from all-sky Gaia photometry (Onken et al. 2019). The wavelengths of SMSS  $griz$  passbands overlap with Gaia and PS1 passbands, so in principle one can tie them together without losing information on the properties of stellar spectra. On the contrary, photometric zero points in  $u$ -band and  $v$ -band remain largely unconstrained due to the lack of short-wavelength passbands in Gaia or PS1.

Panel (a) of Figure 24 shows the mean metallicity distribution of stars ( $1.2 < d < 3$  kpc) from the SMSS in the Galactic coordinate system, which demonstrates the necessity for a second-order photometric zero-point correction. Here, we use metallicities from a fully photometric solution, as it is more prone to photometric errors than the case based on the Gaia parallax. The mean metallicity in each pixel is derived from a generalized histogram of photometric metallicities, which accounts for an uncertainty in metallicity by taking it as a standard deviation of a normal probability distribution. We implement HEALPix (Górski et al. 2005) in the Galactic coordinate system, for which we set a resolution parameter  $N_{\text{side}}$  to 32, corresponding to an equal area of  $3.3 \text{ deg}^2$  for each pixel. Although the bright survey limit restricts the sample to relatively nearby stars, nearly uniform metallicities of stars are contrary to what is expected in the local volume.

To obtain zero-point corrections on SMSS  $uv$  photometry, we assume that nearby stars ( $0.5 < d < 1$  kpc) have the same metallicity in every direction, as they are mostly thin-disk stars. Any deviation in the mean metallicity is attributed entirely to a zero-point error in the  $u$ - and  $v$ -band, because of their larger zero-point uncertainties (Figure 23) and stronger sensitivities on metallicity than other passbands. We also assume the same amount of offset in both passbands. The sensitivity of our metallicity estimate on zero point is estimated using high-latitude stars ( $|b| > 60^\circ$ ) by comparing with a case assuming an arbitrary 0.06 mag offset in the  $u$ - and  $v$ -band, from which we find  $\Delta[\text{Fe}/\text{H}]/\Delta\text{mag} = -2.3$ . Using this factor, the metallicity map is forced to match a reference metallicity ( $[\text{Fe}/\text{H}] = -0.28$ ), which is taken from the average metallicity in the above volume. As shown in panel (b) of Figure 24, we adopt  $N_{\text{side}} = 16$  (a pixel area of  $13.4 \text{ deg}^2$ ) for the zero-point correction map, because a higher spatial resolution results in the loss of some pixels with small numbers of stars, while information on spatial dependence is lost on a lower resolution map. In a new metallicity map based on zero-point corrections [panel (c)], a global change of the mean metallicity from low- to high-latitude regions is evident, as expected from a simple population gradient from the disk to the halo.

For comparison, panel (d) in Figure 24 shows the zero-point corrections in Huang et al. (2021, 2022), who used spectroscopic estimates from the GALAH survey and Gaia parallaxes to derive photometric offsets in each of the SMSS filters. It shows  $u$ -band corrections, but similar patterns and amplitudes are seen in the  $v$ -band. The median difference from our map is negligible (0.004 mag and 0.001 mag in  $u$ - and  $v$ -band, respectively, in the sense of our study minus their values), and a standard deviation amounts to 0.025 mag in both bands. However, high-latitude regions ( $|b| > -50^\circ$ ) are only sparsely populated by GALAH targets, and therefore their correction functions are weakly constrained in the polar regions. In this respect, our correction map provides more complete information for our chemo-kinematic sample along the Galactic prime meridian, which passes through the high-latitude regions.

### B.3. Re-calibration of SDSS $u$ -Band Photometry

In the same manner as for the SMSS  $u$  and  $v$  photometry, SDSS  $u$ -band photometry is re-calibrated for a small, but significant offset in our metallicity map. Panel (a) in Figure 25 shows a mean metallicity distribution from stars at  $1.2 < d < 3$  kpc. There are strips with distinctly lower or higher metallicities than surrounding areas (e.g., the stripe along  $l = 30^\circ$ ; see also Figure 1 in Paper I). These strips are generally parallel to the scanning direction of the SDSS imaging footprints (each  $2.5^\circ$  wide and  $\sim 120^\circ$  long), suggesting that the spatially correlated offsets in metallicity are induced by photometric zero-point errors of the metallicity-sensitive  $u$ -band.

The zero-point correction map in panel (b) is derived in the same way as for the SMSS  $u$  and  $v$  passbands. As there are more stars available for the construction of a metallicity distribution function in SDSS, we adopt a finer pixel size for HEALPix,  $N_{\text{side}} = 32$ . The metallicity sensitivity  $\Delta[\text{Fe}/\text{H}]/\Delta\text{mag} = -2.6$  is obtained from a case with a 0.06 mag offset in  $u$ , and is used to make a uniform metallicity distribution of nearby stars ( $0.5 < d < 1$  kpc) at the ensemble average ( $[\text{Fe}/\text{H}] = -0.25$ ). In this way, only the relative zero-point offsets are rectified, while the global mean remains intact. The revised metallicity map shown in panel (c) is significantly more smooth than in panel (a), and shows no artificial metallicity structures.

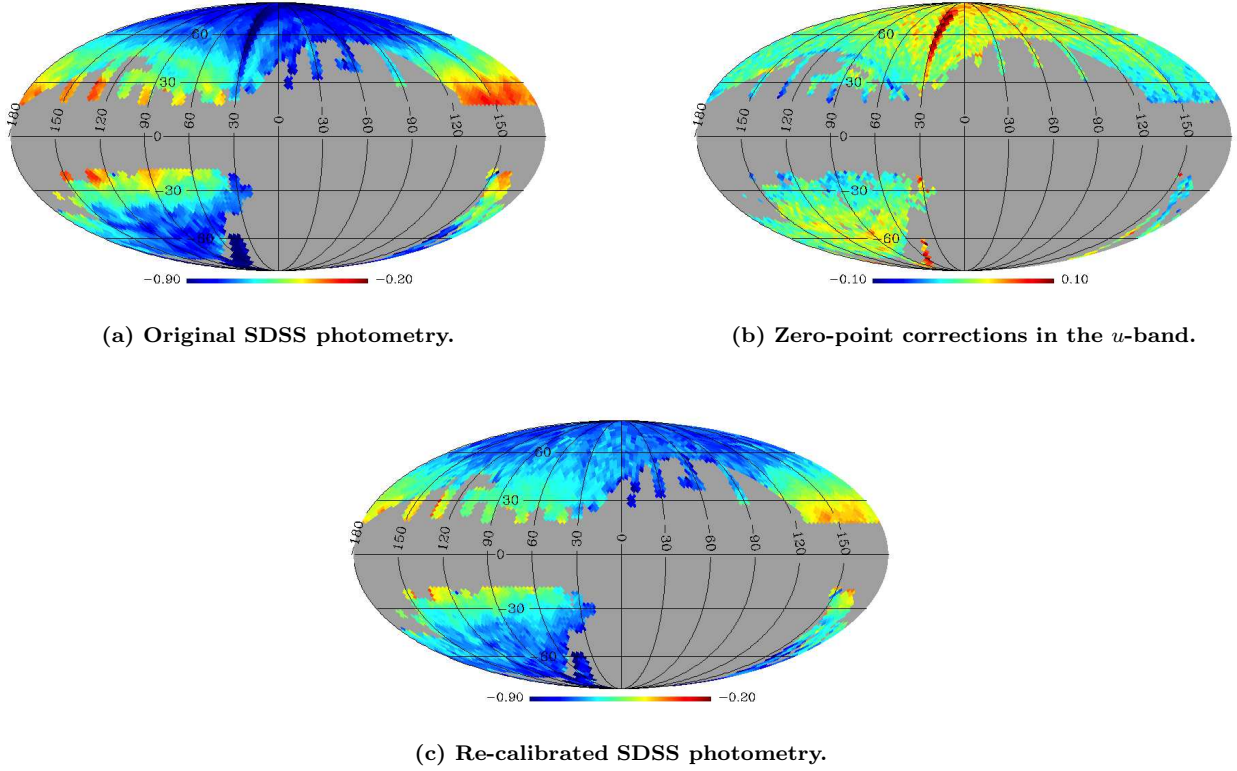


**Figure 25.** Same as in panels (a)–(c) in Figure 24, but from SDSS photometry. Note that the above metallicity maps [panels (a) and (c)] are not exactly same as in Figure 8, owing to different ways of estimating metallicities with and without Gaia parallaxes, respectively.

## REFERENCES

- Abolfathi, B., Aguado, D. S., Aguilar, G., et al. 2018, *ApJS*, 235, 42. doi:10.3847/1538-4365/aa9e8a
- An, D. & Beers, T. C. 2020, *ApJ*, 897, 39. doi:10.3847/1538-4357/ab8d39 (Paper I)
- An, D. & Beers, T. C. 2021a, *ApJ*, 907, 101. doi:10.3847/1538-4357/abccd2 (Paper II)
- An, D. & Beers, T. C. 2021b, *ApJ*, 918, 74. doi:10.3847/1538-4357/ac07a4 (Paper III)
- An, D., Beers, T. C., Johnson, J. A., et al. 2013, *ApJ*, 763, 65. doi:10.1088/0004-637X/763/1/65
- An, D., Beers, T. C., Santucci, R. M., et al. 2015, *ApJL*, 813, L28. doi:10.1088/2041-8205/813/2/L28
- An, D., Johnson, J. A., Clem, J. L., et al. 2008, *ApJS*, 179, 326. doi:10.1086/592090
- An, D., Pinsonneault, M. H., Masseron, T., et al. 2009, *ApJ*, 700, 523. doi:10.1088/0004-637X/700/1/523
- An, D., Pinsonneault, M. H., Terndrup, D. M., et al. 2019, *ApJ*, 879, 81. doi:10.3847/1538-4357/ab23ed
- Bailer-Jones, C. A. L., Rybizki, J., Fouesneau, M., et al. 2021, *AJ*, 161, 147. doi:10.3847/1538-3881/abd806
- Beers, T. C., Carollo, D., Ivezić, Ž., et al. 2012, *ApJ*, 746, 34. doi:10.1088/0004-637X/746/1/34
- Belokurov, V., Erkal, D., Evans, N. W., et al. 2018, *MNRAS*, 478, 611. doi:10.1093/mnras/sty982
- Belokurov, V., Sanders, J. L., Fattahi, A., et al. 2020, *MNRAS*, 494, 3880. doi:10.1093/mnras/staa876
- Belokurov, V. & Kravtsov, A. 2022, *MNRAS*, 514, 689. doi:10.1093/mnras/stac1267
- Bernard, E. J., Ferguson, A. M. N., Schlafly, E. F., et al. 2014, *MNRAS*, 442, 2999. doi:10.1093/mnras/stu1081
- Bessell, M., Bloxham, G., Schmidt, B., et al. 2011, *PASP*, 123, 789. doi:10.1086/660849
- Bessell, M. & Murphy, S. 2012, *PASP*, 124, 140. doi:10.1086/664083
- Bignone, L. A., Helmi, A., & Tissera, P. B. 2019, *ApJL*, 883, L5. doi:10.3847/2041-8213/ab3e0e
- Bohlin, R. C., Gordon, K. D., & Tremblay, P.-E. 2014, *PASP*, 126, 711. doi:10.1086/677655
- Bonaca, A., Conroy, C., Cargile, P. A., et al. 2020, *ApJL*, 897, L18. doi:10.3847/2041-8213/ab9caa

- Bonaca, A., Conroy, C., Wetzel, A., et al. 2017, *ApJ*, 845, 101. doi:10.3847/1538-4357/aa7d0c
- Brook, C., Richard, S., Kawata, D., et al. 2007, *ApJ*, 658, 60. doi:10.1086/511056
- Buck, T. 2020, *MNRAS*, 491, 5435. doi:10.1093/mnras/stz3289
- Buder, S., Sharma, S., Kos, J., et al. 2021, *MNRAS*, 506, 150. doi:10.1093/mnras/stab1242
- Carollo, D., Beers, T. C., Chiba, M., et al. 2010, *ApJ*, 712, 692. doi:10.1088/0004-637X/712/1/692
- Carollo, D., Beers, T. C., Lee, Y. S., et al. 2007, *Nature*, 450, 1020. doi:10.1038/nature06460
- Carretta, E., Gratton, R. G., Clementini, G., et al. 2000, *ApJ*, 533, 215. doi:10.1086/308629
- Casagrande, L., Wolf, C., Mackey, A. D., et al. 2019, *MNRAS*, 482, 2770. doi:10.1093/mnras/sty2878
- Cenarro, A. J., Moles, M., Cristóbal-Hornillos, D., et al. 2019, *A&A*, 622, A176. doi:10.1051/0004-6361/201833036
- Chambers, K. C., Magnier, E. A., Metcalfe, N., et al. 2016, *arXiv e-prints*, arXiv:1612.05560
- Chiappini, C., Matteucci, F., & Gratton, R. 1997, *ApJ*, 477, 765. doi:10.1086/303726
- Cooper, A. P., Parry, O. H., Lowing, B., et al. 2015, *MNRAS*, 454, 3185. doi:10.1093/mnras/stv2057
- Gaia Collaboration, Babusiaux, C., van Leeuwen, F., et al. 2018a, *A&A*, 616, A10. doi:10.1051/0004-6361/201832843
- Gaia Collaboration, Brown, A. G. A., Vallenari, A., et al. 2018b, *A&A*, 616, A1. doi:10.1051/0004-6361/201833051
- Gaia Collaboration, Brown, A. G. A., Vallenari, A., et al. 2021, *A&A*, 649, A1. doi:10.1051/0004-6361/202039657
- Gaia Collaboration, Vallenari, A., Brown, A. G. A., et al. 2022, *arXiv:2208.00211*
- Górski, K. M., Hivon, E., Banday, A. J., et al. 2005, *ApJ*, 622, 759. doi:10.1086/427976
- Grand, R. J. J., Kawata, D., Belokurov, V., et al. 2020, *MNRAS*, 497, 1603. doi:10.1093/mnras/staa2057
- Greener, M. J., Merrifield, M., Aragón-Salamanca, A., et al. 2021, *MNRAS*, 502, L95. doi:10.1093/mnras/lsab012
- Gustafsson, B., Edvardsson, B., Eriksson, K., et al. 2008, *A&A*, 486, 951. doi:10.1051/0004-6361:200809724
- Hayden, M. R., Bovy, J., Holtzman, J. A., et al. 2015, *ApJ*, 808, 132. doi:10.1088/0004-637X/808/2/132
- Haywood, M., Di Matteo, P., Lehnert, M. D., et al. 2013, *A&A*, 560, A109. doi:10.1051/0004-6361/201321397
- Helmi, A. 2020, *ARA&A*, 58, 205. doi:10.1146/annurev-astro-032620-021917
- Helmi, A., Babusiaux, C., Koppelman, H. H., et al. 2018, *Nature*, 563, 85. doi:10.1038/s41586-018-0625-x
- Helmi, A., White, S. D. M., de Zeeuw, P. T., et al. 1999, *Nature*, 402, 53. doi:10.1038/46980
- Henden, A. A., Levine, S., Terrell, D., et al. 2018, *AAS Meeting Abstracts*
- Huang, Y., Yuan, H., Li, C., et al. 2021, *ApJ*, 907, 68. doi:10.3847/1538-4357/abca37
- Huang, Y., Yuan, H., Li, C., et al. 2022, *ApJ*, 924, 141. doi:10.3847/1538-4357/ac425d
- Ivezić, Ž., Kahn, S. M., Tyson, J. A., et al. 2019, *ApJ*, 873, 111. doi:10.3847/1538-4357/ab042c
- Ivezić, Ž., Sesar, B., Jurić, M., et al. 2008, *ApJ*, 684, 287. doi:10.1086/589678
- Kraft, R. P. & Ivans, I. I. 2003, *PASP*, 115, 143. doi:10.1086/345914
- Lee, Y. S., Beers, T. C., Sivarani, T., et al. 2008a, *AJ*, 136, 2022. doi:10.1088/0004-6256/136/5/2022
- Lee, Y. S., Beers, T. C., Sivarani, T., et al. 2008b, *AJ*, 136, 2050. doi:10.1088/0004-6256/136/5/2050
- Lejeune, T., Cuisinier, F., & Buser, R. 1997, *A&AS*, 125, 229. doi:10.1051/aas:1997373
- Lejeune, T., Cuisinier, F., & Buser, R. 1998, *A&AS*, 130, 65. doi:10.1051/aas:1998405
- Lindgren, L., Bastian, U., Biermann, M., et al. 2021, *A&A*, 649, A4. doi:10.1051/0004-6361/202039653
- Mendes de Oliveira, C., Ribeiro, T., Schoenell, W., et al. 2019, *MNRAS*, 489, 241. doi:10.1093/mnras/stz1985
- Myeong, G. C., Belokurov, V., Aguado, D. S., et al. 2022, *arXiv:2206.07744*
- Naidu, R. P., Conroy, C., Bonaca, A., et al. 2020, *ApJ*, 901, 48. doi:10.3847/1538-4357/abaef4
- Naidu, R. P., Conroy, C., Bonaca, A., et al. 2021, *ApJ*, 923, 92. doi:10.3847/1538-4357/ac2d2d
- Necib, L., Ostdiek, B., Lisanti, M., et al. 2020, *Nature Astronomy*, 4, 1078. doi:10.1038/s41550-020-1131-2
- Nissen, P. E., Christensen-Dalsgaard, J., Mosumgaard, J. R., et al. 2020, *A&A*, 640, A81. doi:10.1051/0004-6361/202038300
- Onken, C. A., Wolf, C., Bessell, M. S., et al. 2019, *PASA*, 36, e033. doi:10.1017/pasa.2019.27
- Orkney, M. D. A., Laporte, C. F. P., Grand, R. J. J., et al. 2022, *arXiv:2206.09246*
- Pinsonneault, M. H., Terndrup, D. M., Hanson, R. B., et al. 2004, *ApJ*, 600, 946. doi:10.1086/379925
- Recio-Blanco, A., de Laverny, P., Palicio, P. A., et al. 2022, *arXiv:2206.05541*
- Renaud, F., Agertz, O., Read, J. I., et al. 2021, *MNRAS*, 503, 5846. doi:10.1093/mnras/stab250
- Riello, M., De Angeli, F., Evans, D. W., et al. 2021, *A&A*, 649, A3. doi:10.1051/0004-6361/202039587
- Rockosi, C. M., Lee, Y. S., Morrison, H. L., et al. 2022, *ApJS*, 259, 60. doi:10.3847/1538-4365/ac5323



- Sahlholdt, C. L., Casagrande, L., & Feltzing, S. 2019, *ApJL*, 881, L10. doi:10.3847/2041-8213/ab321e
- Schlafly, E. F. & Finkbeiner, D. P. 2011, *ApJ*, 737, 103. doi:10.1088/0004-637X/737/2/103
- Schlegel, D. J., Finkbeiner, D. P., & Davis, M. 1998, *ApJ*, 500, 525. doi:10.1086/305772
- Sills, A., Pinsonneault, M. H., & Terndrup, D. M. 2000, *ApJ*, 534, 335. doi:10.1086/308739
- Stetson, P. B. 2000, *PASP*, 112, 925. doi:10.1086/316595
- Tonry, J. L., Stubbs, C. W., Lykke, K. R., et al. 2012, *ApJ*, 750, 99. doi:10.1088/0004-637X/750/2/99
- Tonry, J. L., Denneau, L., Flewelling, H., et al. 2018, *ApJ*, 867, 105. doi:10.3847/1538-4357/aae386
- Wolf, C., Onken, C. A., Luvaul, L. C., et al. 2018, *PASA*, 35, e010. doi:10.1017/pasa.2018.5
- Xiang, M. & Rix, H.-W. 2022, *Nature*, 603, 599. doi:10.1038/s41586-022-04496-5
- Yan, Y., Du, C., Liu, S., et al. 2019, *ApJ*, 880, 36. doi:10.3847/1538-4357/ab287d
- Yanny, B., Rockosi, C., Newberg, H. J., et al. 2009, *AJ*, 137, 4377. doi:10.1088/0004-6256/137/5/4377
- Zucker, D. B., Simpson, J. D., Martell, S. L., et al. 2021, *ApJL*, 912, L30. doi:10.3847/2041-8213/abf7cd